Exudate-Guided Janus Trilayer Bioelectronic Dressing for Multimodal Sensing and Therapy of Chronic Wounds

*Canran Yang[1], Qiang Wang[1], Junfeng Yang, Shengwei Shao, Renjie Wang, Chao Luo, Hangwen Li, Jingjie Li and Li Wen**

C. Yang, S. Shao, R. Wang, C. Luo, H. Li, J. Li, L. Wen

Department of Precision Machinery and Precision Instrumentation, University of Science and Technology of China, Hefei, Anhui, 230026, China

E-mail: lilywen@ustc.edu.cn

Q. Wang

The First Affiliated Hospital of USTC, University of Science and Technology of China, Hefei, Anhui, 230001, China

J. Yang

School of Biomedical Engineering, University of Science and Technology of China, Hefei, 230026, China

Keywords: trilayer nanofibrous membrane, gradient wettability, antibacterial drug release, electrical stimulation therapy, multifunctional biosensing, in vivo wound healing, wearable bioelectronics

Abstract

Chronic wounds remain difficult to treat because conventional dressings and systemic therapies are rarely adjusted in real time to the evolving wound microenvironment. Here, we introduce a soft, wearable wound dressing based on a gradient-wettable Janus trilayer fibrous membrane that combines real-time biochemical sensing, on-demand drug release, and low-voltage electrical stimulation. The three vertically stacked layers separately host a multiplex electrochemical sensor array for pH, glucose, and lactate, a silver-sulfadiazine drug reservoir, and stimulation electrodes, while the wettability gradient drives directional exudate transport that sequentially activates each functional layer. The dressing is thin, breathable, stretchable, and intrinsically self-adhesive, enabling conformal contact and stable signal acquisition on

deformable skin without additional tapes. Preclinical tests demonstrate its effectiveness in promoting wound closure, reducing infection, and providing continuous feedback on wound status. This integrated system represents a promising direction for next-generation wound care solutions and regenerative medicine.

1. Introduction

Chronic wounds impact millions of patients worldwide, causing severe health complications and an estimated annual healthcare cost of approximately $26.9 billion in China alone[1-4]. These wounds, including diabetic foot ulcers, stubborn postsurgical wounds, venous ulcers, and burns, are particularly challenging to treat because healing is often impaired or stalled, inflammation stays uncontrolled, and the remodeling of the extracellular matrix (ECM) is dysfunctional[2-6]. While existing clinical interventions like skin grafts, skin substitutes, and negative pressure wound therapy can help promote healing, they tend to be invasive, expensive, and often insufficient complete closure[7]. Infection is another major obstacle, as it can slow down tissue regeneration and lead to tissue death or sepsis[3]. Although local or systemic antibiotics are widely used, their overuse has contributed to the rise of antibiotic resistance, making infections harder to control and increasing risks for patients[8]. In clinical practice, a variety of conventional wound dressings, including gauze, films, foams, hydrogels, alginates, and silver-impregnated materials, are applied to cover wounds, absorb exudate, and help maintain a moist environment. However, these dressings function predominantly as passive barriers, as they lack the capability to monitor or dynamically respond to changes in the wound milieu, offer only limited control over local biochemical cues, and often fail to prevent deterioration or reinfection in chronic, highly exuding wounds, which can necessitate frequent and sometimes painful dressing changes[9-11].

To address these limitations, there is growing interest in advanced wound dressings that can adapt therapeutic intervention to the evolving status of the wound. Real-time monitoring of wound biochemistry is critical for guiding intervention and delivering personalized treatment. Wound exudates contain a wide range of metabolites and indicators, such as pH, glucose, and lactate, which provide direct

insights into tissue repair, inflammation, and infection[12-15]. Wearable electrochemical sensors integrated within wound dressings offer a promising means of continuously converting these biochemical changes at the wound interface into quantitative electrical signals. However, the complex and dynamic composition of wound fluids creates significant challenges for such sensors, particularly in terms of long-term stability, selectivity, and reliable operation in vivo[13, 16, 17]. Meanwhile, electrical stimulation therapy has gained attention because it can facilitate fibroblast growth, boost collagen production, promote keratinocyte migration, and support new blood vessel formation[18, 19]. Nonetheless, electrical stimulation alone cannot fully eliminate infection risks, and traditional delivery of antibiotics often results in uncontrolled dosing and can speed up resistance development[8, 20]. Combining real-time biochemical sensing with synergistic therapies, including localized drug delivery and electrical stimulation, presents a promising but still largely unfulfilled strategy for precise, adaptive wound management. These ongoing challenges emphasize the urgent need for next-generation wound dressings that go beyond passive protection to actively manage the wound microenvironment, dynamically tailor therapy based on real-time biochemical feedback, and integrate versatile therapeutic functions within a single, multifunctional platform.

Building on these clinical needs, recent years have seen rapid progress in flexible and wearable bioelectronic dressings. A variety of single-layer, planar systems have been reported in which electrochemical sensors, heaters, or electrical stimulation electrodes are patterned on hydrogel or elastomer substrates to monitor pH, temperature, pressure, or selected metabolites and, in some cases, to deliver drugs or electrical cues at the wound site[14, 21-23]. However, because all functions are confined to one planar substrate, these devices often face trade-offs between mechanical compliance, sensing performance, and therapeutic output, and their essentially two-dimensional layouts limit spatial utilization and make further increases in multifunctionality difficult. In addition, many electronic dressings are built on continuous polymer films or plastic foils that are only weakly breathable and lack intrinsic adhesion to tissue, which can lead to sweat or exudate accumulation and

unstable contact under motion, so additional tapes or bandages are required for fixation, which can compromise comfort and long-term stability on irregular, moving skin. Handling wound exudate remains particularly challenging: in many reported designs, exudate must be collected and routed through predefined microfluidic channels to reach the sensing regions, requiring precise control over droplet capture and channel geometry and increasing the risk of clogging, device failure, and fabrication complexity[24, 25]. Ideally, wound dressings should not only create a breathable environment, prevent secondary infections, and efficiently remove excess fluids, but also support real-time sensing, controlled drug release, and precise stimulation all within a single, integrated platform[14, 20, 26]. Achieving such comprehensive integration in a structurally simple, mechanically compliant, and clinically practical dressing remains a formidable challenge.

Instead of relying solely on conventional planar or single-layer integration strategies, we developed a multifunctional, wearable wound dressing platform based on electrospun Janus membranes with multilayer heterogeneous structures. In contrast to recently reported integrated dressings[20, 22, 27], where sensing, drug release, and stimulation are often confined within one hydrogel layer or co-planar film, our design distributes each functional module along the vertical direction in distinct fiber layers, , namely an inner hydrophobic TPU–PSA contact layer that is intrinsically self-adhesive and mechanically robust, an intermediate amphiphilic TPU–PVP–PSA drug reservoir with an interconnected porous network, and an outer superhydrophilic HPAN sensing layer formed by ultrafine fibers. This vertically graded architecture produces a thin, stretchable and conformal membrane whose fibrous network remains highly breathable while providing strong yet skin-friendly adhesion and efficient exudate handling. The resulting hierarchical Janus membrane exhibits an asymmetric wettability profile that enables rapid, unidirectional lifting and removal of wound exudate away from the wound bed. This not only maintains a non-macerating and oxygen-permeable microenvironment that is conducive to tissue regeneration, but also turns the inevitable vertical transport of exudate into a cascading activation mechanism for the stacked functional layers. As exudate is continuously wicked

upward, it first permeates the inner adhesive contact layer that hosts the stimulation electrodes, where low-voltage electrical fields are applied across the wound interface, then gradually reaches the intermediate drug-loaded layer, where silver sulfadiazine is released adaptively along the concentration gradient, and finally arrives at the top sensing layer, where electrochemical monitoring is triggered in a timely manner. By coupling vertical fluid transport with spatially separated functional modules, the trilayer Janus membrane not only overcomes key limitations of single-layer systems but also makes more efficient use of the available footprint, enabling high-density integration and miniaturization of sensing and stimulation elements while preserving mechanical flexibility. In this vertically stratified configuration, wound exudate is maximally exploited as both a transport medium and an activation trigger, and the membrane provides an integrated yet modular platform that can be readily extended with additional functional layers for simultaneous exudate management, therapy, and real-time biochemical sensing[20, 22, 26].

2. Results and Discussion

2.1. Design of the gradient-wettable Janus trilayer fibrous dressing

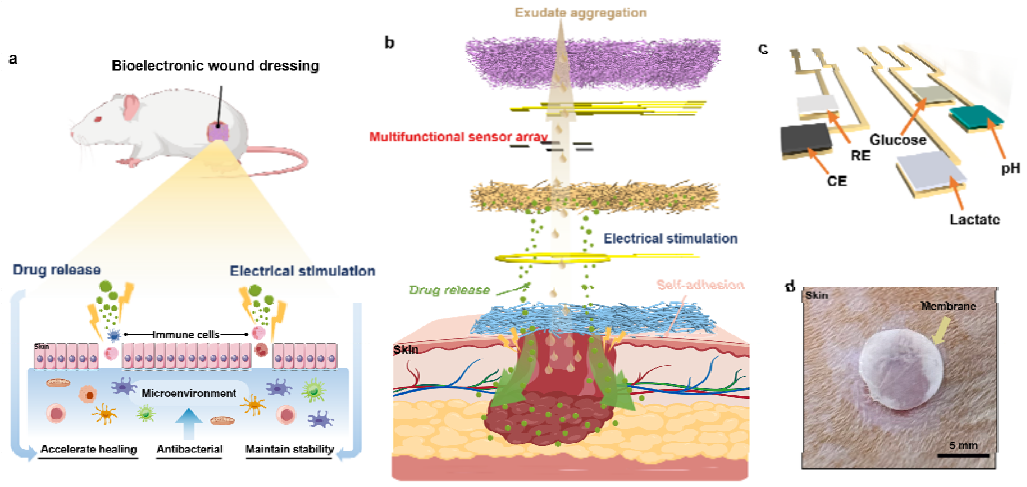

Figure 1. Gradient-wettable trilayer bioelectronic dressing architecture and wound-healing mechanism. a) Schematic illustration of the wound-healing mechanism. The dressing accelerates tissue repair by synergistically modulating the wound microenvironment through localized drug release and electrical stimulation. **b)** In situ schematic of the multifunctional dressing. Exudate wetting triggers Ag

release to inhibit bacterial growth, while low-voltage electrical stimulation promotes tissue regeneration. Simultaneously, an integrated multisensor array continuously analyzes key biochemical markers in the exudate to monitor wound status. **c)** Schematic illustration of the electrochemical sensing array for multiplexed analysis of wound biomarkers. **d)** An optical image of the dressing conformally adhered to a murine dorsal wound, demonstrating stable attachment during the healing process.

In this work, we introduce a soft, gradient-wettable Janus trilayer wound dressing platform that seamlessly integrates real-time biochemical sensing, localized drug delivery, and electrical stimulation therapy within a single fibrous substrate **(Figures 1a, b)**. The trilayer membrane consists of an inner hydrophobic self-adhesive TPU-PSA contact layer that hosts the stimulation electrodes, an intermediate amphiphilic TPU-PVP-PSA drug-reservoir layer, and an outer highly hydrophilic HPAN sensing layer. The vertically graded wettability confers a Janus character, in which wound exudate is wicked upward against gravity from the wound bed through the hydrophobic adhesive layer, then into the intermediate amphiphilic drug-loaded layer, and finally into the outer hydrophilic sensing layer. Low-frequency electrical stimulation is applied through the electrodes embedded in the inner contact layer at the wound interface and promotes cell migration, alignment, and tissue repair[17]. In this vertically stratified configuration, exudate primarily activates the drug and sensing layers. When the fluid front reaches the amphiphilic drug reservoir, it hydrates the silver-sulfadiazine layer and triggers concentration-gradient-driven release, so localized anti-inflammatory and antimicrobial treatment occurs only when exudate is present. When exudate recedes and the drug layer is no longer infiltrated, diffusion is effectively suppressed, which produces a self-limiting mode of controlled drug release[20, 22]. As exudate subsequently wets the hydrophilic sensing layer, the sensor films are activated and multiplex electrochemical monitoring of pH, glucose, and lactate can be performed under the chemically complex conditions of wounds **(Figure 1b, c)** [14, 20, 26]. The overall fabrication sequence of the integrated bioelectronic dressing is summarized in **Figure S1** and described in detail in the Experimental

Section. Briefly, a PAN solution is first electrospun and hydrolyzed to form the HPAN fibrous layer, which serves as the outer sensing substrate. Gold-based electrodes for glucose, lactate, and pH sensing are patterned onto the HPAN surface, and the corresponding enzyme and pH-sensitive films are deposited to define the sensor array. Next, a TPU–PVP–PSA solution containing silver sulfadiazine is electrospun to form the amphiphilic drug-loaded middle layer. Electrical stimulation electrodes are then defined by magnetron sputtering onto the drug-loaded intermediate layer. Finally, a TPU–PSA solution is electrospun to form the inner hydrophobic self-adhesive contact layer, and flexible interconnects are attached to the electrode pads, resulting in a fully integrated trilayer bioelectronic dressing that can be conformed to the skin surface.

At the same time, its porous fibrous network allows air and water vapor to pass through, helping to maintain a non-macerating microenvironment that supports wound healing **(Figure 1d)**[14, 22, 28]. Systematic evaluation in animal models showed that this integrated platform allows for multimodal biomarker tracking, significantly accelerates the healing of chronic wounds, and effectively reduces infection and inflammation[14, 17, 20, 22, 26, 27].

Taken together, this work not only demonstrates a gradient-wettable Janus trilayer dressing that couples exudate-guided, layer-by-layer activation of drug release and sensing with soft electrical stimulation, but also establishes a generalizable framework for the design of multifunctional bioelectronic dressings for tissue repair and regenerative medicine.

2.2. Construction and Characterization of the Gradient-Wettable Janus Trilayer Membrane

Guided by the design considerations above, we constructed and characterized the gradient-wettable Janus trilayer membrane that serves as the substrate of the multifunctional dressing. The three functional modules for sensing, drug release, and electrical stimulation are embedded in a single electrospun fibrous scaffold with a vertically graded architecture. The innovative design of the dressing leverages electrospinning, a cost-effective and versatile technique[26, 27, 29, 30], enabling precise control over fiber diameter[31] and pore size[24] by modulating key parameters such as

polymer solution concentration[21], applied voltage[32], feed rate[33] and deposition time[34]. Furthermore, selecting materials with specific physical properties enables the tailoring of distinct membrane characteristics[35, 36].

From the perspective of practical wound care, the fibrous scaffold should be thin, soft, and stretchable in order to match the mechanics of skin. It should also be self-adhesive so that it remains in place without additional tapes and sufficiently breathable to prevent maceration. At the same time, efficient removal of exudate from the wound bed is required to limit bacterial growth and biochemical fluctuations. These multiple requirements are difficult to achieve with a single homogeneous layer, so we designed a vertically graded trilayer architecture in which each layer is optimized for a specific function and together they form an integrated Janus-type dressing. The inner layer is designed as a hydrophobic, highly adhesive and mechanically robust contact layer that anchors the dressing to irregular skin and supports the stimulation electrodes. The intermediate layer serves as an amphiphilic drug reservoir with an interconnected porous network that can store silver-based antimicrobials and release them in response to exudate-driven concentration gradients. The outer layer is composed of finer and more hydrophilic fibers that promote rapid wicking and spreading of exudate away from the wound surface and facilitate water vapor transport. By selecting polymers and compositions with appropriate wettability, elasticity, adhesiveness, and pore structures for each layer, the resulting trilayer membrane provides stretchability, conformal adhesion, breathability, and directional exudate management within a single integrated construct.

To implement this architecture, we finely tuned the polymer formulations and electrospinning conditions for each layer to obtain a trilayer micro and nanofibrous membrane with well defined porosity and a hydrophobic to amphiphilic to superhydrophilic wettability gradient, which underpins its directional fluid transport and stable adhesion. As illustrated in **Figure 2a**, a polyacrylonitrile (PAN) solution was first electrospun into a fibrous membrane and then hydrolyzed in an alkaline solution to obtain hydrolyzed PAN (HPAN). This treatment introduced hydrophilic functional groups (–COOH, –CONH) to the fibers, which endowed the HPAN layer

with superhydrophilicity and markedly enhanced wettability (**Figures S2** and **S3**). Subsequently, thermoplastic polyurethane (TPU) blended with polyvinylpyrrolidone (PVP) and pressure sensitive adhesive (PSA) (TPU-PVP-PSA) was electrospun onto the HPAN substrate to form the middle amphiphilic, self-adhesive layer. Finally, a TPU-PSA solution was electrospun as the third layer, yielding a more hydrophobic and highly adhesive fibrous surface that enhances the mechanical integrity of the membrane and provides strong interfacial bonding between the membrane and skin. With this sequential electrospinning process and an appropriate orientation during use, the resulting dressing presents an inner TPU-PSA contact layer, a middle TPU-PVP-PSA layer, and an outer HPAN layer, giving rise to distinct yet well integrated porosity and wettability gradients.

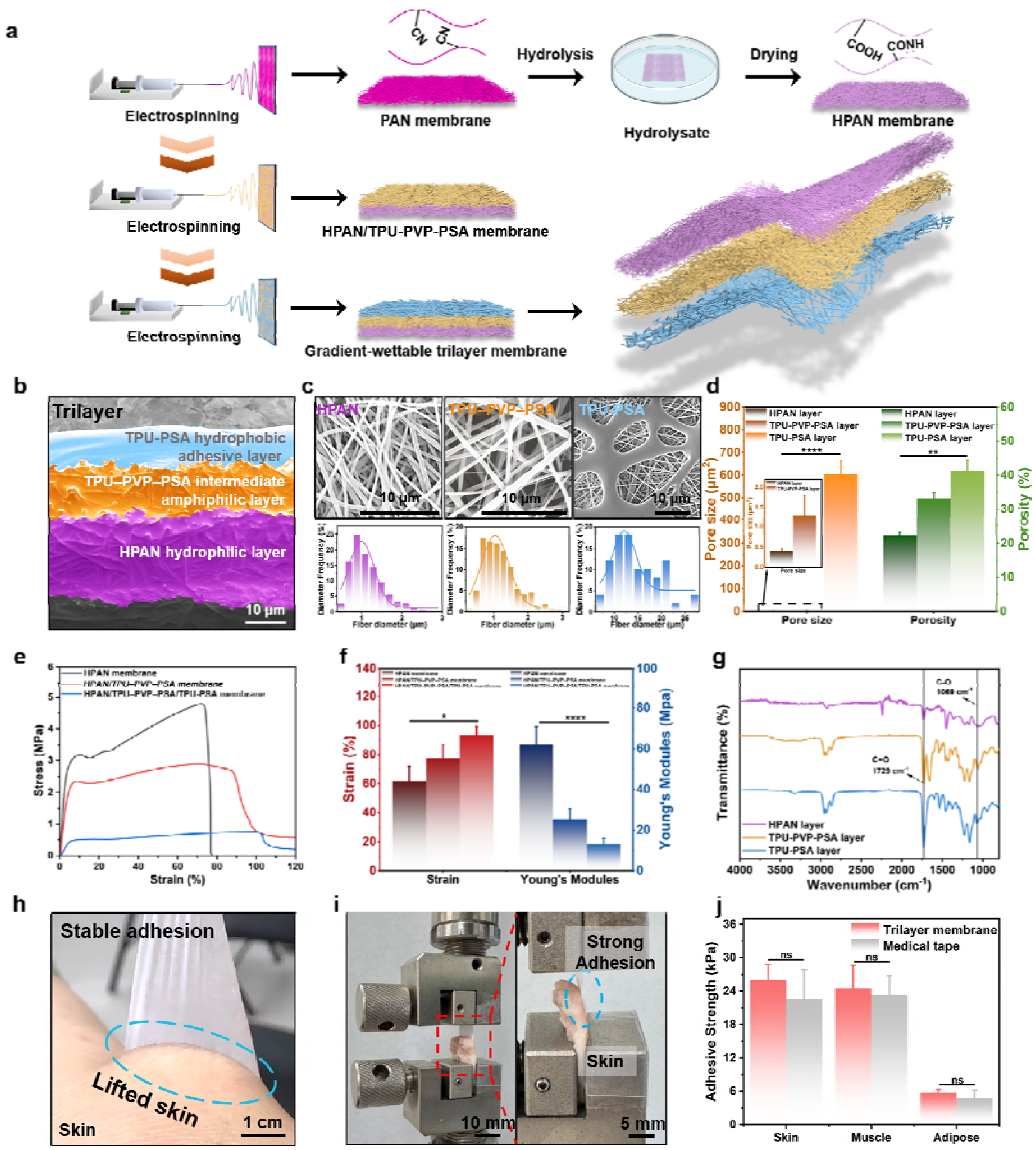

Figure 2. Structural configuration and properties of the gradient-wettable trilayer membrane. a) Schematic of the fabrication process involving sequentially electrospinning TPU–PVP–PSA and TPU–PSA layers onto a hydrolyzed PAN nanofibrous membrane (HPAN membrane). **b**) Cross-sectional SEM image of the gradient-wettable trilayer membrane showing distinct layered architecture. HPAN layer (purple), TPU–PVP–PSA layer (orange), TPU–PSA layer (blue). **c**) SEM images and corresponding fiber diameter distributions of HPAN layer, TPU–PVP–PSA layer and TPU–PSA layer. **d**) Comparison of average pore size and porosity across layers (**P < 0.01; ****P < 0.0001; n = 3). **e**) Representative stress–strain curves of stepwise-assembled monolayer (HPAN layer), bilayer (HPAN and TPU–PVP–PSA

layers) and trilayer (HPAN, TPU–PVP–PSA and TPU–PSA layers) membranes. **f**) Comparison of tensile strain and Young's modulus across stepwise-assembled monolayer, bilayer and trilayer membranes (*$P < 0.05$; ****$P < 0.0001$; $n = 3$). **g**) FTIR spectra of individual layers showing key functional-group peaks that confer distinct adhesion and wettability characteristics. **h**) A optical image showing stable adhesion of the trilayer membrane to skin. **i**) Mechanical peel test on porcine skin demonstrating strong adhesion. **j**) Quantitative comparison of adhesion strength on porcine skin, muscle, and adipose tissues (ns $p \geq 0.05$; $n = 3$). Error bars represent mean ± SD.

Figure 2b presents a cross-sectional SEM image of the trilayer membrane, showing the HPAN layer (purple), TPU-PVP-PSA layer (orange), and TPU-PSA layer (blue) are distinctly identifiable. This ultrathin membrane exhibits a remarkably low mass of 0.0071 g and a thickness of only 0.048 mm **(Figure S4**), rendering it promising for imperceptible wear on skin surfaces[37, 38]. Morphological analysis of individual layers is presented in **Figure 2c**. SEM images reveals continuous and bead-free fibers across all layerswith fiber diameter distributions progressively increasing from the HPAN (1.0 μm) to the TPU-PVP-PSA (1.3 μm) and TPU-PSA (14.7 μm) layers. These variations in fiber diameter directly impact pore size and porosity, establishing a hierarchical structure that facilitates directional water transport from the wound-facing inner TPU-PSA layer through the intermediate TPU-PVP-PSA layer to the outer HPAN surface, which is crucial for effective exudate management in wound care.

To quantitatively characterize the fibrous architecture of the multilayer membrane, mean pore size and porosity of individual layers are analyzed in **Figure 2d**. The TPU-PSA layer exhibits the largest pore size (603.6 μm^2) and the highest porosity (41.4%), followed by TPU-PVP-PSA (1.3 μm^2, 33.8%) and HPAN (0.4 μm^2, 22.2%). This pore gradient is vital for creating a capillary-driven fluid transport pathway, ensuring efficient exudate management while preventing maceration and inflammation.

The mechanical behavior of the trilayer assembly was evaluated through tensile testing. As shown in **Figure 2e**, the sequential incorporation of the TPU-PVP-PSA and TPU-PSA layers onto the HPAN substrate progressively reduced structural stiffness while enhancing extensibility. The standalone HPAN layer exhibited limited extensibility (71% strain at break) and relatively high tensile strength (47.9 MPa). In contrast, the trilayer architecture achieved a pliable mechanical profile, combining superior stretchability (101.8% strain at break) with lower tensile strength (7.6 MPa). This transition from a rigid to a more flexible material profile is critical for improving the comfort and long-term wearability of the dressing on dynamic skin surfaces, particularly in chronic wound management. Quantitative comparison of the maximum strain and Young's modulus for sequentially assembled membranes is presented in **Figure 2f**. The mean strain capacity increased from 62.1% to 93.5%, accompanied by a substantial reduction in Young's modulus from 61.8 MPa to 13.0 MPa. This engineered transition from a rigid to compliant mechanical profile is critical for biomedical interfaces, as it significantly mitigates interfacial stress concentration at the skin-device junction. The enhanced compliance minimizes shear-induced delamination during dynamic movement, thereby improving wear comfort and long-term adhesion stability for chronic wound management.

Fourier-transform infrared (FTIR) spectroscopy of individual layers (**Figure 2g**) reveals critical functional groups governing interfacial interactions. The characteristic peaks at ≈1729 cm^{-1} (C=O stretching of urethane/ester groups)[39, 40] and ≈1069 cm^{-1} (C–O stretching of ether/alcohol moieties)[41] indicate hydrogen-bonding capable sites[42]. Notably, the TPU-PSA layer exhibits the highest peak intensities at these positions, followed by TPU-PVP-PSA and HPAN. This gradient in polar group density directly correlates with adhesion strength. The TPU-PSA layer maximizes skin contact through abundant hydrogen-bonding sites, enabling conformal attachment to human tissue. The intermediate TPU-PVP-PSA layer provides strong interfacial adhesion to both adjacent layers, preventing trilayer membrane delamination via cooperative polar interactions. Collectively, this chemically-graded architecture ensures structural integrity.

To further evaluate the tissue adhesion capability of the trilayer membrane, we performed peel-off tests on ex vivo porcine tissues. **Figure 2h** demonstrates pronounced skin deformation during peel-off testing, where skin visibly elevates with membrane detachment, confirming robust interfacial bonding. Quantitative mechanical assessments of porcine tissues in **Figure 2i** reveal that the trilayer membrane exhibits adhesive strengths comparable to standard medical tape across skin, muscle and adipose tissue (**Figure 2j**). Standard medical tape exhibited adhesive strengths of 22.6 kPa, 23.4 kPa, and 4.8 kPa when attached to porcine skin, muscle, and adipose tissue, respectively. In contrast, the trilayer membrane achieved adhesive strengths of 26.0 kPa, 24.5 kPa, and 5.8 kPa on the identical tissue substrates, with no statistically significant difference between the two groups. Although the high oil content of adipose tissue reduces adhesion for both materials, the membrane still meets clinical adhesion requirements on skin and muscle[43]. Importantly, despite its strong adhesion, the membrane can be removed cleanly from human skin without leaving residue or causing epidermal damage, as shown in **Figure S5**, demonstrating exceptional biocompatibility. This unique combination of strong yet safe adhesion, coupled with conformal adaptability to heterogeneous tissue morphologies, ensures secure biomedical device fixation with minimized iatrogenic injury risks during chronic use.

2.3. Dual-gradient Trilayer Membrane for Enhanced Wound Fluid Management and Antimicrobial Delivery

To comprehensively assess the multifunctional capabilities of the gradient-wettable trilayer membrane for wound management, we systematically investigated its tissue adhesion, directional fluid transport, gradient-driven wettability modulation, and controlled passive drug release. These integrated features collectively determine its therapeutic efficacy in dynamic wound environments.

As depicted in **Figure 3a**, the trilayer membrane demonstrates excellent mechanical compliance upon application to wrinkled human skin. It maintains intimate, gap-free contact without delamination or buckling, preserving the topographic details of the underlying skin. This wrinkle-conforming capability is

critical for reliable biosignal acquisition and sustained therapeutic delivery, particularly in dynamic dermatological interfaces[44, 45]. **Figure 3b** illustrates the asymmetric wettability structure enabling unidirectional fluid transport. The gradient structure consists of a hydrophilic HPAN outer layer, an amphiphilic TPU-PVP-PSA intermediate layer, and a hydrophobic TPU-PSA inner layer. This architecture establishes a capillary-driven fluid transport mechanism that lifts wound exudate from the wound bed to the exterior while preventing the ingress of external contaminants. The mechanism underlying this directional transport is governed by Laplace pressure dynamics within the fibrous membrane (**Figure 3c** and **Figure S6**). Upon contact with the membrane, droplets enter capillary channels formed between fibers and are subjected to Laplace pressure, which is expressed as:

$$P = \frac{4\gamma \cos\theta}{D} \tag{1}$$

where γ is the liquid–gas interfacial tension, θ is the contact angle on the fiber surface, and D is the pore diameter. The decreasing contact angle (from the inner TPU-PSA to the outer HPAN layer) and the progressively smaller pore size contribute to the increasing capillary pressure in the outward direction. This dual gradient in wettability and pore structure increases the capillary pressure in the outward direction, enabling the pressure difference to overcome gravitational and viscous forces and drive fluid unidirectionally from the inner hydrophobic layer toward the outer hydrophilic layer. In this way, the trilayer membrane continuously lifts wound exudate away from the wound bed while limiting the inward penetration of external contaminants, thereby reducing the risk of maceration and infection.

Figure 3d shows the time-dependent wetting behavior of individual layers and the integrated trilayer membrane through sequential contact angle measurements using 3 μL droplets. The hydrophilic HPAN layer transitions rapidly from an initial contact angle of 22° to complete wetting within 9 seconds. The TPU-PVP-PSA layer, optimized at a 1:1 ratio for balanced amphiphilicity (**Figure S7**), exhibits gradual wetting kinetics, transitioning from 92° to 0° over 66 seconds. In contrast, the hydrophobic TPU-PSA layer maintains stability with contact angles near 120°

throughout the measurement period. In the trilayer configuration, the water contact angles evolve from 118° to full wetting at 47 seconds, demonstrating the progressive liquid penetration from the tissue-facing interior to the hydrophilic exterior. These distinct wetting dynamics, quantitatively shown in **Figure 3f**, establish a temporal wettability gradient that combines rapid exterior wetting with persistent interior hydrophobicity, facilitating directional fluid transport and consistent with capillary-driven mechanisms. Moreover, this hierarchical structure ensures superior moisture vapor transmission rates (MVTR = 5.7 $kg \cdot m^{-2} \cdot d^{-1}$, **Figure S8**) compared to conventional PDMS substrates[22] under 50°C and 30% RH. By preventing fluid accumulation while maintaining optimal oxygen permeability, the membrane avoids the formation of hypoxic microenvironments that impede angiogenesis and epithelial regeneration[46].

To complement the dynamic wetting analysis, 3 μL water droplets were deposited separately onto each individual layer (HPAN, TPU-PVP-PSA and TPU-PSA) and onto the wound-facing TPU-PSA side of the complete trilayer membrane. **Figure 3e** presents top-view optical images of 3 μL droplet spreading after 5 minutes of static contact. The hydrophilic HPAN outer layer exhibits near-complete wetting with extensive droplet spreading, while the hydrophobic TPU-PSA inner layer shows minimal spreading due to its non-wetting properties. The amphiphilic TPU-PVP-PSA intermediate layer displayed moderate spreading behavior between these two extremes. When the droplet was placed on the hydrophobic inner surface of the trilayer membrane (TPU-PSA side), the projected wetting area on the surface was smaller than that on the HPAN monolayer but the liquid penetrated through all three layers, indicating through-thickness transport across the full trilayer membrane rather than simple surface spreading on the hydrophobic layer. Quantitative analysis in **Figure 3g** shows that the HPAN outer layer reached the largest spreading area (24.41 mm^2), followed by the trilayer membrane, where a droplet deposited on the hydrophobic TPU-PSA side obtained an overall apparent spreading area of 12.39 mm^2 across the full membrane, while the TPU-PVP-PSA layer showed only limited spreading (0.25 mm^2) and the TPU-PSA layer exhibited negligible wetting (0 mm^2).

This asymmetric liquid handling capacity, characterized by unidirectional drainage and a persistent hydrophobic barrier on the wound-facing side, ensures effective exudate management while preventing retrograde contaminant ingress.

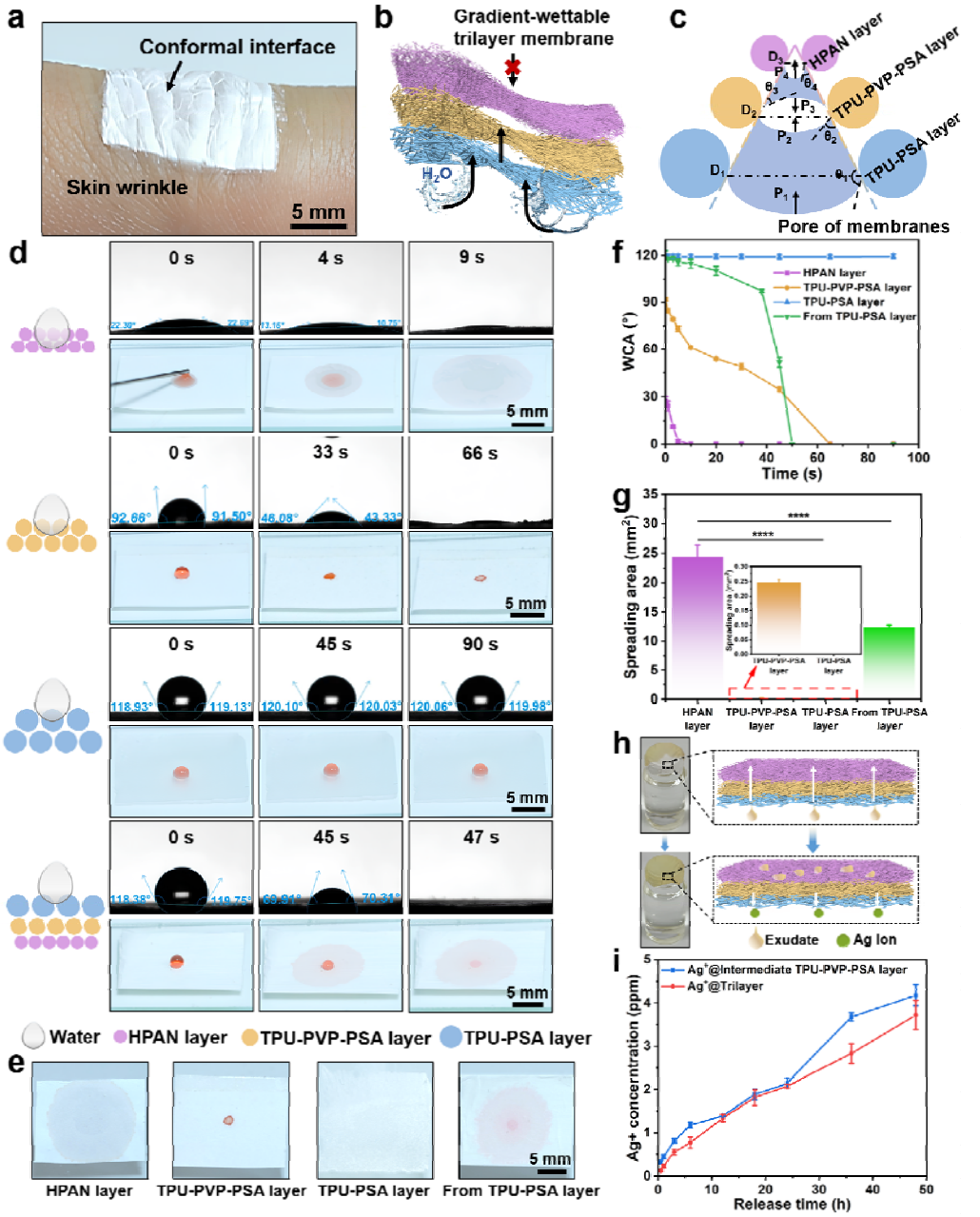

Figure 3. Directional liquid transport and controlled antimicrobial drug release enabled by a gradient-wettable trilayer membrane. a) Conformal adhesion and mechanical compliance of the trilayer membrane on wrinkled skin surfaces. **b)** Schematic illustration of the hierarchical trilayer fibrous architecture featuring

unidirectional fluid transport and anti-reverse permeation. **c)** Schematic of mechanism underlying unidirectional fluid transport from the hydrophobic TPU-PSA layer to the hydrophilic HPAN layer across the trilayer membrane. **d)** Optical images showing initial 3 μL water droplet contact angles on the hydrophobic adhesive TPU-PSA layer, intermediate amphiphilic TPU-PVP-PSA layer, hydrophilic HPAN layer, and the complete trilayer membrane from TPU-PSA layer. **e)** Top-view optical images depicting the spreading behavior of 3 μL water droplets after 5 minutes on each individual layer and the trilayer membrane. **f)** Water contact angle (WCA) of each individual layer and complete trilayer membrane from hydrophobic TPU-PSA layer at different times (n = 3). **g)** Quantitative analysis of 3 μL water droplet spreading areas after 5 minutes across each individual layer and trilayer membrane (****$P < 0.0001$; n = 3). **h)** Schematic and corresponding optical images of unidirectional transport of exudates and directional release of Ag^{+} ions through the trilayer membrane. **i)** Quantitative analysis of cumulative release profiles of Ag^{+} ions from the single intermediate amphiphilic layer and the trilayer membrane over 48 hours (n = 3). Error bars represent mean ± SD.

Beyond fluid management, antimicrobial agents are essential for preventing wound infections[20, 24]. In this study, silver sulfadiazine was incorporated into the intermediate TPU-PVP-PSA layer. Energy-dispersive X-ray spectroscopy (EDS) mapping of this layer (**Figure S9**) shows that Ag, N and O signals are homogeneously distributed throughout the fibrous network, indicating uniform loading of silver sulfadiazine without obvious aggregation. When wound exudate permeates this amphiphilic region, Ag^{+} ions from silver sulfadiazine diffuse toward the wound bed along a concentration gradient[47, 48]. **Figure 3h** schematically illustrates this directional ion release toward the wound interface. Notably, the gradient-wettability architecture spatially separates fluid and ion transport pathways. Wound exudate is rapidly wicked outward through capillary-driven flow, whereas Ag^{+} ions released from silver sulfadiazine in the hydrated middle layer diffuse back toward the wound interface along the concentration gradient through the fibrous network. This spatial

and temporal decoupling between fluid drainage and ion transport slows Ag^{+} depletion at the wound surface and helps to sustain an effective antimicrobial level over extended periods. Quantitative analysis in 10 mL 0.1× PBS (**Figure 3i**) demonstrates ion release kinetics. The intermediate single-layer releases 4.2 ppm Ag^{+} at 48 hours, while the trilayer releases 3.7 ppm, maintaining therapeutic concentrations above the 0.1 ppm bactericidal threshold[49, 50]. This confirms that the hydrophobic inner and hydrophilic outer layers do not significantly compromise ion diffusion, while still ensuring antimicrobial efficacy. This confirms that the additional hydrophobic inner and hydrophilic outer layers do not impede Ag^{+} diffusion and that the trilayer architecture maintains effective antimicrobial levels while directing exudate away from the wound. By coupling directional fluid drainage with sustained silver release, the membrane establishes a stable, infection-resistant microenvironment that is favorable for tissue repair. On this basis, we further integrated and characterized multiplexed electrochemical sensors and electrical stimulation electrodes on the trilayer membrane to achieve real-time monitoring and active modulation of the wound microenvironment.

2.4. Design and characterization of a multiplexed sensor array for biomarker analysis and electrical stimulation

Benefiting from the interconnected micro/nanofibrous network and the designed gradients in pore size and surface wettability of the trilayer membrane, it drives wound exudate preferentially from the skin-facing interface toward the outer surface, providing directional transport while limiting reverse permeation and local fluid accumulation. On this vertically organized scaffold, the wound dressing integrates a multiplexed sensor array for the electrochemical detection of biomarkers in wound exudate, a pair of electrodes for electrical stimulation to promote cell proliferation and wound healing, and a gradient-wettable trilayer fibrous membrane whose intermediate layer serves as a drug reservoir loaded with anti-inflammatory and antimicrobial drugs. The trilayer membrane provides a soft, adhesive and breathable structural substrate that supports both the sensor array and the stimulation electrodes while maintaining stable contact with the wound surface.

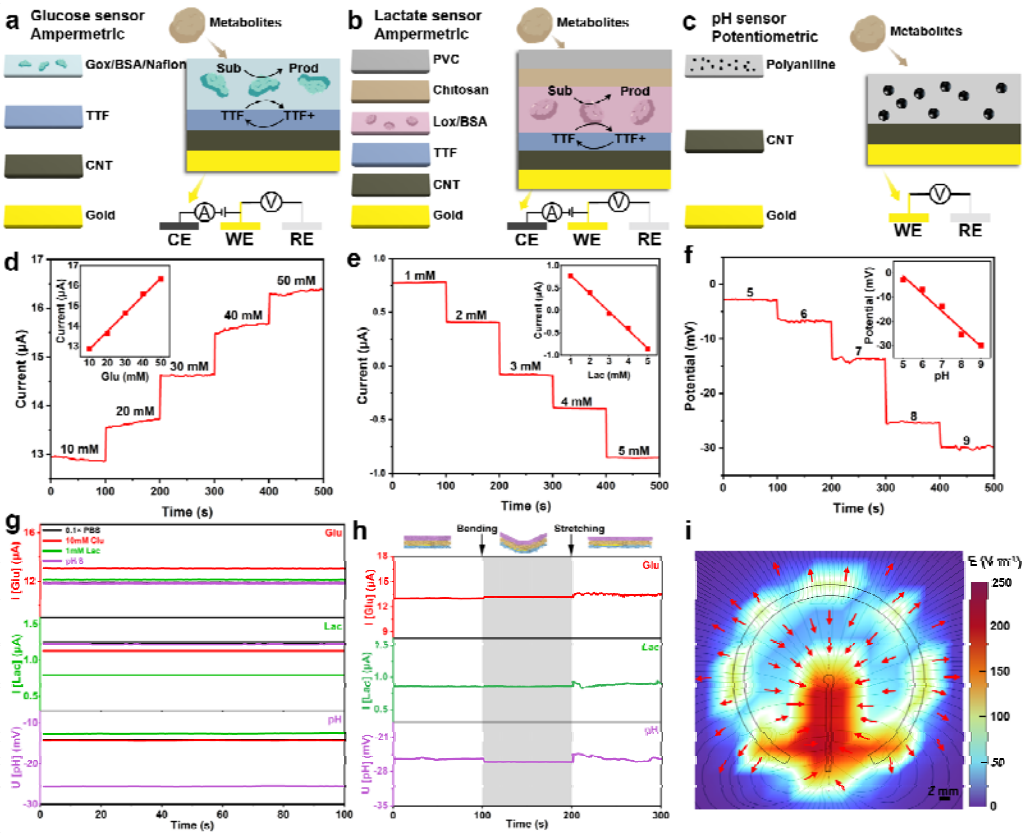

Figure 4. Characterization of the multiplexed electrochemical sensing array and electrical stimulation electrodes in the trilayer bioelectronic dressing. a-c) Schematics of the enzymatic **(a)** glucose and **(b)** lactate sensors and the potentiometric **(c)** pH sensor. Gox, glucose oxidase; BSA, Bovine Serum Albumin; TTF, tetrathiafulvalene; CNT, carbon nanotube; Sub, substrate; Prod, product; PVC, polyvinyl chloride; Lox, lactate oxidase; CE, counter electrode; WE, working electrode; RE, reference electrode. **d-f)** Chronoamperometric responses of the enzymatic **(d)** glucose, **(e)** lactate sensors and potentiometric response of the **(f)** pH sensor, the calibration plots with a linear fit. **g)** Selectivity study of the sensors. Time-dependent responses recorded in separate measurements where 50 μL of 0.1× PBS, 10 mM glucose, 1 mM lactate, or pH 8 standard buffer was individually added onto the sensors; each curve corresponds to one test solution. **h)** Responses of the sensors before and during mechanical bending (radius 1 cm) and mechanical stretching (10%) in 0.1× PBS (pH 7) containing 10 mM glucose and 1 mM lactate. **i)** Numerical simulation of the electrical field generated by the custom-designed

electrical stimulation electrodes during operation. E, electrical field.

The multiplexed sensor array is designed for real-time monitoring of key biochemical markers in wound exudate. Continuous and selective measurements of glucose, lactate and pH are particularly important for evaluating the healing status of wounds[14, 51]. In our system, glucose and lactate are detected by amperometric enzymatic electrodes in which glucose oxidase (GOx) or lactate oxidase (LOx) catalyze the oxidation of the corresponding substrate to generate hydrogen peroxide or reduced mediator species. At a fixed applied potential versus the Ag/AgCl reference electrode, these redox processes produce a Faradaic current that is proportional to the local analyte concentration. The pH is monitored by a potentiometric electrode coated with a polyaniline based sensing film whose protonation state varies with the hydrogen ion activity at the interface, giving rise to a potential that follows a near linear dependence on pH (**Figures 4a–c**). To achieve stable and selective operation in the chemically complex environment of wound exudate, the sensing interfaces are further engineered at the material level. Tetrathiafulvalene (TTF) combined with carbon nanotubes (CNTs) forms a conductive composite membrane that immobilizes GOx and LOx and facilitates rapid electron transfer, which improves both enzymatic stability and reaction kinetics[52]. For the glucose sensor, GOx is additionally embedded in a bovine serum albumin (BSA) and Nafion matrix that acts as an ion diffusion limiting layer, thereby enhancing linearity and sensitivity while suppressing interference from electroactive species[53]. For lactate, which diffuses more rapidly due to its smaller molecular size, chitosan is incorporated to construct a denser diffusion limiting layer and extend the usable linear range [54]. These tailored interfacial structures are integrated on the outer HPAN layer of the trilayer membrane, where the gradient wettability ensures that wound exudate is continuously lifted toward the sensing surface and replenished by fresh fluid. This configuration improves analyte accessibility and sampling efficiency compared with planar dressings that rely on lateral spreading of exudate on a flat substrate.

The electrochemical performance of the three sensors is summarized in **Figures**

4d–f. The glucose electrode exhibits a monotonic increase in steady state current with increasing glucose concentration, whereas the lactate electrode shows a monotonic decrease in current with increasing lactate concentration, reflecting the opposite polarity of the applied potential used for the two enzymatic reactions. Both sensors display highly linear calibration curves over the tested concentration range, with correlation coefficients of 0.998 and −0.998 and sensitivities of 0.088 μA mM^{-1} and −0.406 μA mM^{-1} for glucose and lactate, respectively. The pH sensor produces a nearly linear potential response to solution pH with a correlation coefficient of −0.986 and a sensitivity of −7.278 mV pH^{-1}, which is adequate for resolving the clinically relevant pH changes associated with infection and inflammation. All three sensors employ Ag/AgCl coated electrodes as reference electrodes to maintain a stable potential[55]. The high linearity and reproducible sensitivities of all three channels indicate that the sensor array can reliably distinguish subtle variations in glucose, lactate and pH. Together with the conformal, self-adhesive and breathable trilayer membrane, these sensing characteristics provide a robust basis for multiplex biochemical monitoring directly at the wound interface.

Wound exudate contains a complex mixture of metabolites that may potentially interfere with sensor readings. To evaluate the selectivity of the three sensors, their responses to both target and non-target metabolites were tested. As shown in **Figure 4g**, negligible responses were observed when non-target metabolites were introduced, while the corresponding target metabolites elicited significant sensor signals. Notably, short-term fluctuations in environmental pH did not significantly affect the amperometric glucose and lactate sensor responses (**Figure S10**). The operational stability of the three sensors was further assessed by repeated measurements. In these tests, 5 μL aliquots of test solution were repeatedly dropped onto the sensing area, measured, removed and replaced with fresh solution in successive cycles. As shown in **Figure S11**, the responses recorded before and after repeated operation exhibited only minor changes for the pH sensor, and the glucose and lactate sensor signals remained largely unchanged, demonstrating good stability and reproducibility during prolonged use.. Furthermore, due to the flexible fibrous membrane substrate, the wound dressing

conformed well to the skin and maintained intimate contact during skin movements. Mechanical bending and 10% uniaxial stretching (**Figure 4h**), as well as repeated bending cycles (**Figure S12**) did not produce significant changes in the responses of any of the three sensors, further demonstrating the mechanical reliability and stability of the system.

To further promote tissue regeneration, a directional electric field was applied through the stimulation electrodes using a 1 V, 50 Hz voltage signal (**Figure 4i**, and **Figures S13-S14**). Figure 4i presents a numerical simulation of the electrical field generated by the custom-designed electrical stimulation electrodes. The simulation results show uniform distribution of the electric field across the wound surface, confirming the effectiveness of the stimulation in promoting cell migration and tissue repair. **Figures S13 and S14** provide a detailed breakdown of the electrical stimulation system. **Figure S13** shows the circuit diagram, while **Figure S14** displays the optical image of the system integrated on a flexible printed circuit board (FPCB), as well as the voltage profile showing a programmed 10-minute stimulation phase followed by a 20-minute rest period. The representative stimulation waveform during the working phase, delivering a 1 V, 50 Hz signal, is also shown, illustrating the sustained electrical stimulation provided to the wound interface. Numerous previous studies have shown that externally applied electric fields can modulate cell migration, orientation of cell division, and other cellular behaviors, thereby enhancing tissue regenerative capacity[19, 56-59]. On the basis of these characterizations, we further evaluated the therapeutic efficacy and real-time monitoring capability of the integrated dressing in vivo using rodent wound models.

2.5. In vivo assessment of the wound dressing in a murine model

We first evaluated the in vitro biocompatibility of the trilayer membrane, which showed no detectable cytotoxicity with or without drug loading (**Figure S15**). These results indicate that the membrane does not adversely affect cell viability and is suitable for further in vivo investigation. Building on these findings, we applied the trilayer wound dressing to a full-thickness dorsal skin defect model in rats (**Figure 5a**). Compared with the control group, the drug-loaded trilayer dressing markedly

accelerated wound contraction and epithelialization, which can provide a compliant adhesive interface that supports cell adhesion and migration. The addition of electrical stimulation further amplified the therapeutic effect, consistent with the well-established role of applied electric fields in guiding the migration and proliferation of keratinocytes and fibroblasts[60, 61]. After 11 days of treatment, the drug-and-electrical-stimulation (drug & ES) dressing achieved a wound closure rate of 95.27%, outperforming both the drug-only dressing (87.48%) and the control group (80.96%) (**Figure 5b, e**, and **Figures S16-S18**). Hematoxylin–eosin (HE) staining of the regenerated tissue (**Figure 5c**) confirmed these macroscopic observations. In the drug & ES group, the wound area is covered by a continuous, stratified epidermal layer with a well organized dermal structure and dense granulation tissue, whereas in the drug-only and control groups residual scab, surface edema and discontinuous or thinner epidermis can still be observed. Quantitative analysis shows that the epidermis is substantially thicker in the drug & ES group (55.88 μm) than in the drug-only group (26.18 μm) and the control group (12.95 μm) (**Figure 5f**), indicating more advanced re-epithelialization and tissue remodeling under the combined biochemical and electrical stimulation.

To further evaluate the pathological characteristics of the regenerated tissue, Masson and α-SMA immunohistochemical staining were performed on wound samples from the different treatment groups. The results showed that wounds treated with the drug- and electrically stimulated trilayer dressing exhibited the highest collagen area at 73.38%, significantly higher than the drug-only dressing group at 65.94% and the untreated control group at 47.35%. Similarly, the α-SMA-positive area, indicative of myofibroblast presence and tissue remodeling, was highest in the drug- and electrically stimulated trilayer dressing group at 16.72%, followed by the drug-only dressing group at 13.85%, and the control group at 10.32% (**Figure 5d, g**). These findings suggest that the combined biochemical and electrical stimulation not only promotes collagen deposition but also enhances myofibroblast activation, thereby accelerating tissue remodeling and recovery during the early healing phase. Concurrently, to investigate the dynamics of wound-related biochemical parameters

under infected and uninfected conditions, we further monitored the concentrations of glucose and lactate, as well as the pH of both wound models (**Figure 5h-j** and **Figures S19-S22**). Throughout the 5-day observation period, infected and uninfected wounds exhibited distinct differences in glucose, lactate, and pH values. Consistent with previous reports, infected wounds showed lower glucose concentrations[(62)], elevated lactate levels[(63)], and an increase in pH[(64, 65)]. However, transient increases in lactate and pH observed in the uninfected group could be attributed to the normal inflammatory response or local microenvironmental fluctuations that induce mild, transient inflammation. Notably, the peaks of lactate and pH typically appeared on postoperative day 2 or 3, corresponding to the inflammatory phase in which large numbers of leukocytes infiltrate the injury site[(2, 66)]. After this period, both parameters exhibited a gradual decline in infected and uninfected wounds. Although the infected wounds maintained relatively higher values, the continuous downward trend suggests progressive healing, likely due to the antibacterial activity of the trilayer dressing.

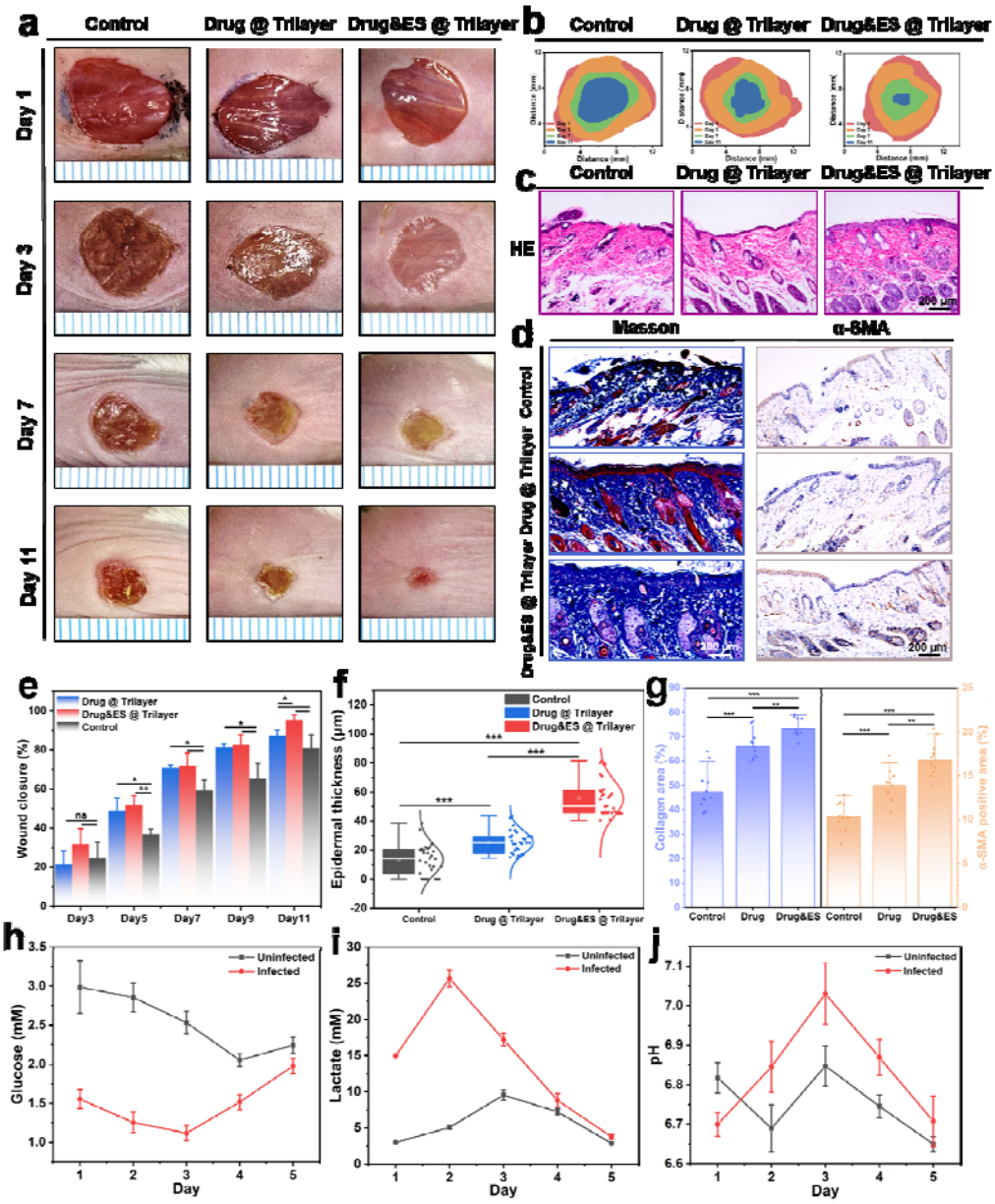

Figure 5. Preliminary in vivo evaluation of the trilayer wound dressing for skin repair. a) The representative photographs of wound healing with different treatment groups on days 1, 3, 7, and 11. **b)** The wound trace of these groups. **c)** HE staining images of wound samples. **d)** Staining of Masson and α-SMA in various treatment groups. **e)** Statistical results of wound closure rates on days 3, 5, 7, 9, and 11 (*P < 0.05; **P < 0.01; n = 3). **f)** The epidermal thickness of repair areas in different treatment groups (**P < 0.01; ***P < 0.001; n = 30). **g)** Expression area of collagen (Masson) and α-SMA in various treatment groups (**P < 0.01; ***P < 0.001; n = 12).

h-j) Continuous monitoring of the **(h)** glucose, **(i)** lactate, and **(j)** pH of the infected/uninfected wounds during the healing process (n = 3). Error bars represent mean ± SD.

Above all, these in vivo results indicate that the trilayer dressing not only accelerates wound closure and improves tissue regeneration but also enables dynamic monitoring of wound status by continuously tracking key biochemical parameters. Such real-time insight into the healing trajectory has considerable potential to guide future personalized therapeutic strategies.

3. Discussion

In this work, we developed a fully integrated wound dressing that incorporates biosensing, electrical stimulation and controlled drug release within a trilayer asymmetric fibrous membrane. The system enables comprehensive and continuous monitoring of wound biochemical indicators while simultaneously accelerating tissue repair. The non-symmetric structure effectively transports exudate from the wound bed to the outer surface, which prevents excessive moisture, maceration and inflammation. The breathable and biocompatible fibrous membrane further provides a stable foundation for the integration of multiple functional modules. During the vertical transport process, wound exudate infiltrates the drug-loaded middle layer. The resulting concentration gradient drives the diffusion of antibacterial agents toward the injury site, producing effective antimicrobial and anti-inflammatory activity. In addition, the spatial arrangement of the electrical stimulation component facilitates localized field delivery, which promotes cell migration and proliferation and ultimately enhances wound contraction. Meanwhile, the biosensing layer utilizes the elevated exudate to perform reliable glucose, lactate and pH measurements under complex and dynamic wound conditions without interrupting the healing process.

Compared with conventional dressings, this trilayer system offers a rare combination of breathability, mechanical flexibility, therapeutic support and multi-parameter biochemical monitoring. The modular design also provides significant potential for customization. Different sensing components or therapeutic

units can be incorporated to meet the needs of diverse clinical scenarios. This adaptability suggests that the platform may provide a practical route toward personalized wound care, improved treatment precision and better clinical decision-making in the future.

4. Methods

4.1. Materials

All reagents and materials were used as received unless otherwise specified. Polyacrylonitrile (PAN), thermoplastic polyurethane (TPU), polyvinylpyrrolidone (PVP), pressure-sensitive adhesive (PSA), silver sulfadiazine, glucose oxidase (GOx), lactate oxidase (LOx), bovine serum albumin (BSA), tetrathiafulvalene (TTF), carbon nanotubes (CNTs), Nafion, chitosan, uric acid (UA), hydrochloric acid, anhydrous glucose, phosphate-buffered saline (PBS), polyaniline (PANI), and polyvinyl chloride (PVC) were purchased from Aladdin. Ultrapure water (18.2 MΩ·cm) was used for solution preparation. Dimethylformamide (DMF) was used as the solvent for electrospinning. PANI and PVC were obtained from Shanghai Acmec Biochemical Technology Co., Ltd. All other reagents were also sourced from Shanghai Acmec Biochemical Technology Co., Ltd.

4.2. HPAN layer

A 2 wt% PAN solution in DMF was prepared and electrospun under a voltage of 16 kV with the collector at –2 kV, a tip-to-collector distance of 13 cm, and a flow rate of 0.02 μL min^{-1}. The as-spun PAN membrane was hydrolyzed in a NaOH solution (3 g NaOH in 15 mL deionized water and 65 mL ethanol) at 50 °C for 15 min to obtain hydrolyzed PAN (HPAN). The HPAN membrane was dried under vacuum at 40 °C for 1 h prior to subsequent use.

4.3. TPU-PVP-PSA intermediate layer

A mixed solution containing 8.43 wt% TPU, 8.43 wt% PVP, and 33.3 wt% PSA in DMF was prepared and sonicated for 3 h to ensure homogeneity. Electrospinning was performed at 14 kV (collector at –2 kV), a tip-to-collector distance of 13 cm, and a flow rate of 0.035 μL min^{-1}.

4.4. TPU-PSA layer

A solution containing 9.0 wt% TPU and 50.0 wt% PSA in DMF was prepared and sonicated for 3 h. Electrospinning was conducted at 12.5 kV (collector at –2 kV), a tip-to-collector distance of 13 cm, and a flow rate of 0.04 μL min^{-1}.

4.5. Electrospinning environment

All electrospinning processes were performed at 50 °C and 40% relative humidity, using an electrospinning machine (TEADFS-100, Beijing Technova Technology Co., Ltd.)

4.6. Drug Loading

Silver sulfadiazine (AgSD) was incorporated into the TPU–PVP–PSA intermediate layer by adding it directly into the solution during preparation. Specifically, 0.5 g of AgSD was added for every 4.4 g of TPU and PVP. The mixture was stirred at 65 °C until it was fully homogenized.

4.7. Structural and Chemical Characterization

The surface and cross-sectional morphologies of the membranes were observed using scanning electron microscopy (SEM) (Zeiss EVO 18). Fiber diameters and pore sizes were measured from SEM images using ImageJ software (NIH). Fourier transform infrared (FTIR) spectra were recorded in transmission mode on a Nicolet iN10 instrument, with a scanning range from 4000 to 400 cm^{-1}. Water contact angles were determined using a goniometer (Biolin Scientific Theta Flex) by placing 3 μL droplets on the membrane surface. Mechanical properties, including tensile strength, were tested using an Instron universal testing machine (Instron 5566, Shimadzu EZ-LX) at a strain rate of 2 mm min^{-1}. Young's modulus and strain at break were calculated from the stress–strain curves. The water evaporation rate was measured using a YG501B tester (Wenzhou Fangyuan Instrument Co., Ltd.) based on the GB/T12704.2-2009 standard. Moisture permeability tests were performed at 38 ± 2 °C and 50 ± 2 % relative humidity. The release of silver ions (Ag^{+}) from the membrane was quantified using inductively coupled plasma-mass spectrometry (ICP-MS, iCAP RQ). Surface chemical composition and elemental states were analyzed by X-ray photoelectron spectroscopy (XPS, Kratos AXIS SUPRA+).

4.8. Fabrication of Patterned Electrodes

Aluminum plates were patterned using a UV picosecond laser cutter (LSP30) to create electrode masks. The electrodes for the electrostimulation and sensing modules were then fabricated via magnetron sputtering (SP-SC4-A00).

4.9. Fabrication of Sensor Arrays

pH Sensor

The pH sensor was based on a polyaniline (PANI) film electrochemically polymerized onto a carbon nanotube (CNT) paper. The working electrode was cleaned by cyclic voltammetry (CV) in 0.5 M HCl with 10 cycles (scan rate: 0.1 V s^{-1}, potential range: −0.1 to 0.9 V). PANI electro-polymerization was performed in a 50 μL solution containing 0.1 M aniline and 1 M HCl using 50 CV cycles (−0.2 to 1.2 V, scan rate: 0.1 V s^{-1}). The CNT paper was then adhered to the gold (Au) electrode using conductive silver paste. The electrodes were air-dried at 4°C overnight.

Glucose Sensor

A 0.1 M PBS solution was prepared by diluting 5 mL of 1× PBS with 45 mL deionized water. To fabricate the CNT electrode pad, 1 μL of a 0.1 M tetrathiafulvalene (TTF) solution (0.02 g TTF dissolved in 1 mL anhydrous ethanol) was drop-cast onto the pad. The enzyme coating solution was prepared by dissolving 40 mg/mL glucose oxidase (GOx) in 0.1 M PBS containing 10 mg/mL bovine serum albumin (BSA), with a final GOx concentration of 100 mg/mL. A 1 wt% Nafion solution was prepared by mixing 1 mL of 5% Nafion with 1 mL anhydrous ethanol, followed by dilution to 2 mL with 0.1 M PBS. The Nafion solution was mixed in equal volume with the enzyme solution and drop-cast onto the TTF-coated CNT pad. The CNT pad was then adhered to a gold current collector using conductive silver paste, and the assembly was cured at 4°C for 24 hours. The electrodes were stored at 4°C for at least 1 week to allow the Nafion membrane to equilibrate.

Lactate Sensor

The lactate sensor was fabricated following a similar procedure to the glucose sensor. In addition to the glucose oxidase (GOx) enzyme layer, a 3 μL chitosan solution (prepared by dissolving 1% chitosan in 2% acetic acid and stirring for 1 hour) was drop-cast onto the electrode surface. After the chitosan layer, 3 μL of polyvinyl

chloride (PVC) solution was applied on top of the chitosan layer.

Reference Electrode

The Ag/AgCl reference electrode was prepared by directly applying Ag/AgCl gel onto a gold electrode and allowing it to air dry.

Counter Electrode

For the counter electrode, a 10% platinum-carbon (Pt/C) suspension (10 mg/mL) was prepared in a 2 wt% Nafion ethanol solution. 5 μL of the Pt/C suspension was drop-cast onto the current collector.

4.10. In vitro cell studies

Cell Lines

NIH-3T3 fibroblasts were cultured under 37°C and 5% CO_2. Cells were passaged at 70% confluency, with passages 3 to 5 used for all studies.

In vitro biocompatibility and Proliferation Studies

Electroactive hydrogels were washed and transferred to 24-well cell culture inserts. NIH-3T3 fibroblasts were seeded at a density of 1×10^{4} cells per well. The inserts were placed in 24-well plates, and cells were incubated with appropriate media at 37°C and 5% CO_2. Cell proliferation and viability were assessed using a commercial PrestoBlue assay (Thermo Fisher Scientific) to evaluate metabolic activity. For cell viability, a calcein AM/ethidium homodimer-1 live/dead kit (Invitrogen) was used. Live cells were stained green with calcein-AM, and dead cells were stained red with ethidium homodimer-1. The percentage of live cells was calculated using ImageJ software by determining the ratio of live cells to total cells.

4.11. In Vivo Wound Healing Model

Animal Model

In vivo studies were conducted on Sprague-Dawley rats (female) to assess the wound healing efficacy of the trilayer dressing. The rats were anesthetized with isoflurane (2-3% in oxygen), and full-thickness dorsal skin defects (0.8 cm diameter) were induced on their backs.

Wound Closure and Epithelialization

The wound closure rate was quantified by analyzing the wound area using image

processing. Epithelialization and epidermal thickness were evaluated using hematoxylin and eosin (HE) staining. The epidermal thickness was measured on histological sections from the wound area.

Histological Staining and Analysis

To assess tissue remodeling and myofibroblast activation, histological staining for α-SMA and Masson trichrome was performed on tissue sections. Sections were incubated with primary antibodies specific for α-SMA, and Masson trichrome was used to stain collagen. The expression levels of α-SMA and the percentage of collagen-positive areas were quantified using ImageJ. The areas of positive staining were calculated to determine myofibroblast presence and collagen content, providing insights into tissue regeneration and inflammation during the wound healing process.

Animal Infection Model

5 μL of Staphylococcus aureus (S. aureus) bacterial solution was applied to the wound site on the dorsal area of the mice five times. After each application, the solution was allowed to air dry before the next application.

Biochemical Parameter Monitoring

Wound fluid samples were collected for continuous biochemical analysis of glucose, lactate, and pH. The concentrations were measured using biosensors integrated into the dressing. Glucose and lactate were monitored using specific sensors, and pH was measured using a pH sensor. Wound fluid was collected daily for 5 days, and parameters were recorded at regular intervals to track the biochemical changes during healing.

Acknowledgments

The authors acknowledge the Experimental Center of Engineering and Material Sciences at University of Science and Technology of China for the fabrication and measuring of samples. This work was partially carried out at Instruments Center for Physical Science, University of Science and Technology of China. The authors are also grateful to their colleagues for their essential contribution to this study.

Funding: This work has been funded by the National Natural Science Foundation of China (No. 51375469), the Fundamental Research Funds for the Central Universities

(WK5290000003).

Author contributions: C.R.Y.: Writing – original draft, Visualization, Validation, Project administration, Methodology, Investigation, Funding acquisition, Formal analysis, Data curation, Conceptualization, Writing – review & editing. Q.W.: Visualization, Validation, Methodology, Investigation, Formal analysis, Data curation. J.F.Y. and S.W.S: Investigation, Formal analysis, Data curation. R.J.W., C.L., H.W.L and J.J.L: Formal analysis. L.W.: Writing – original draft, Supervision, Funding acquisition, Formal analysis.

Competing interests: The authors declare that they have no known competing financial interests or personal relationships that could have appeared to influence the work reported in this paper.

Data availability: All data needed to support the conclusions of this manuscript are included in the main text and the supplementary information/source data file and are available from the corresponding authors upon request.

References

1. D. Queen, K. Harding, What's the true costs of wounds faced by different healthcare systems around the world? *Int Wound J* **20**, 3935-3938 (2023).
2. M. Rodrigues, N. Kosaric, C. A. Bonham, G. C. Gurtner, Wound Healing: A Cellular Perspective. *Physiol Rev* **99**, 665-706 (2019).
3. L. E. Tracy, R. A. Minasian, E. J. Caterson, Extracellular Matrix and Dermal Fibroblast Function in the Healing Wound. *Adv Wound Care* **5**, 119-136 (2016).
4. S. A. Eming, P. Martin, M. Tomic-Canic, Wound repair and regeneration: Mechanisms, signaling, and translation. *Sci Transl Med* **6**, (2014).
5. D. G. Armstrong, A. J. M. Boulton, S. A. Bus, Diabetic Foot Ulcers and Their Recurrence. *New Engl J Med* **376**, 2367-2375 (2017).
6. M. E. Shaydakov, W. Ting, M. Sadek, F. Aziz, J. A. Diaz, J. D. Raffetto, W. A. Marston, B. K. Lal, H. J. Welch, A. V. F. R. Comm, Review of the current evidence for topical treatment for venous leg ulcers. *J Vasc Surg-Venous L* **10**, 241-247 (2022).
7. P. Saramago, A. Gkekas, C. E. Arundel, I. C. Chetter, S.-T. Investigators, Negative pressure wound therapy for surgical wounds healing by secondary intention is not cost-effective. *Bjs-Brit J Surg* **112**, (2025).
8. B. Aslam, W. Wang, M. I. Arshad, M. Khurshid, S. Muzammil, M. H. Rasool, M. A. Nisar, R. F. Alvi, M. A. Aslam, M. U. Qamar, M. K. F. Salamat, Z. Baloch, Antibiotic resistance: a rundown of a global crisis. *Infect Drug Resist* **11**, 1645-1658 (2018).

9. R. N. Dong, B. L. Guo, Smart wound dressings for wound healing. *Nano Today* **41**, (2021).
10. M. Farahani, A. Shafiee, Wound Healing: From Passive to Smart Dressings. *Adv Healthc Mater* **10**, (2021).
11. W. Zhang, L. L. Liu, H. Cheng, J. Zhu, X. Y. Li, S. Ye, X. J. Li, Hydrogel-based dressings designed to facilitate wound healing. *Mater Adv* **5**, 1364-1394 (2024).
12. P. Mostafalu, A. Tamayol, R. Rahimi, M. Ochoa, A. Khalilpour, G. Kiaee, I. K. Yazdi, S. Bagherifard, M. R. Dokmeci, B. Ziaie, S. R. Sonkusale, A. Khademhosseini, Smart Bandage for Monitoring and Treatment of Chronic Wounds. *Small* **14**, (2018).
13. M. Q. Wang, Y. R. Yang, J. H. Min, Y. Song, J. B. Tu, D. Mukasa, C. Ye, C. H. Xu, N. Heflin, J. S. McCune, T. K. Hsiai, Z. P. Li, W. Gao, A wearable electrochemical biosensor for the monitoring of metabolites and nutrients. *Nat. Biomed. Eng.* **6**, 1225-1235 (2022).
14. E. S. Sani, C. H. Xu, C. R. Wang, Y. Song, J. H. Min, J. B. Tu, S. A. Solomon, J. H. Li, J. L. Banks, D. G. Armstrong, W. Gao, A stretchable wireless wearable bioelectronic system for multiplexed monitoring and combination treatment of infected chronic wounds. *Sci Adv* **9**, (2023).
15. X. Zhang, R. Lv, L. Chen, R. Sun, Y. Zhang, R. Sheng, T. Du, Y. Li, Y. Qi, A Multifunctional Janus Electrospun Nanofiber Dressing with Biofluid Draining, Monitoring, and Antibacterial Properties for Wound Healing. *ACS Appl Mater Interfaces* **14**, 12984-13000 (2022).
16. C. R. Wang, K. X. Fan, E. S. Sani, J. A. Lasalde-Ramírez, W. Z. Heng, J. H. Min, S. A. Solomon, M. Q. Wang, J. H. Li, H. Han, G. Kim, S. Shin, A. Seder, C. D. Shih, D. G. Armstrong, W. Gao, A microfluidic wearable device for wound exudate management and analysis in human chronic wounds. *Sci Transl Med* **17**, (2025).
17. C. X. Shi, H. Wang, X. J. Wang, K. F. Li, P. B. Liu, L. H. Wang, H. Yu, A Safe, Stable, Simple, Serviceable, and Self-Powered Wound Dressing With Continuous Low-Voltage Direct Current Electrical Stimulation: an Efficient Approach to Accelerate Wound Healing. *Adv Funct Mater* **35**, (2025).
18. Q. Y. Peng, Y. Qian, X. X. Xiao, F. D. Gao, G. Q. Ren, C. P. Pennisi, Advancing Chronic Wound Healing through Electrical Stimulation and Adipose-Derived Stem Cells. *Adv Healthc Mater* **14**, (2025).
19. M. Zhao, B. Song, J. Pu, T. Wada, B. Reid, G. P. Tai, F. Wang, A. H. Guo, P. Walczysko, Y. Gu, T. Sasaki, A. Suzuki, J. V. Forrester, H. R. Bourne, P. N. Devreotes, C. D. McCaig, J. M. Penninger, Electrical signals control wound healing through phosphatidylinositol-3-OH kinase-γ and PTEN. *Nature* **442**, 457-460 (2006).
20. Y. R. Liu, S. F. Huang, S. Y. Liang, P. R. Lin, X. J. Lai, X. Z. Lan, H. Wang, Y. D. Tang, B. T. Gao, Phase Change Material-Embedded Multifunctional Janus Nanofiber Dressing with Directional Moisture Transport, Controlled Release of Anti-Inflammatory Drugs, and Synergistic Antibacterial Properties. *Acs*

Appl Mater Inter **15**, 52244-52261 (2023).
21. S. Wang, N. N. Wang, D. Kai, B. F. Li, J. Wu, J. C. C. Yeo, X. W. Xu, J. Zhu, X. J. Loh, N. Hadjichristidis, Z. B. Li, In-situ forming dynamic covalently crosslinked nanofibers with one-pot closed-loop recyclability. *Nat Commun* **14**, (2023).
22. B. Chen, B. He, A. M. Tucker, I. Biluck, T. H. Leung, T. P. Schaer, S. Yang, An Environmentally Stable, Biocompatible, and Multilayered Wound Dressing Film with Reversible and Strong Adhesion. *Adv Healthc Mater* **13**, (2024).
23. G. Xu, Y. L. Lu, C. Cheng, X. Li, J. Xu, Z. Y. Liu, J. L. Liu, G. Liu, Z. H. Shi, Z. T. Chen, F. N. Zhang, Y. X. Jia, D. F. Xu, W. Yuan, Z. Cui, S. S. Low, Q. J. Liu, Battery-Free and Wireless Smart Wound Dressing for Wound Infection Monitoring and Electrically Controlled On-Demand Drug Delivery. *Adv Funct Mater* **31**, (2021).
24. X. M. Zhang, R. J. Lv, L. X. Chen, R. M. Sun, Y. Zhang, R. T. Sheng, T. Du, Y. H. Li, Y. F. Qi, A Multifunctional Janus Electrospun Nanofiber Dressing with Biofluid Draining, Monitoring, and Antibacterial Properties for Wound Healing. *Acs Appl Mater Inter* **14**, 12984-13000 (2022).
25. H. B. Wang, M. J. Wang, X. H. Xu, P. Gao, Z. L. Xu, Q. Zhang, H. Y. Li, A. X. Yan, R. Y. T. Kao, H. Z. Sun, Multi-target mode of action of silver against Staphylococcus aureus endows it with capability to combat antibiotic resistance. *Nat Commun* **12**, (2021).
26. Y. P. Dong, S. J. Fu, J. Y. Yu, X. R. Li, B. Ding, Emerging Smart Micro/Nanofiber-Based Materials for Next-Generation Wound Dressings. *Adv Funct Mater* **34**, (2024).
27. S. T. Qian, J. Wang, Z. M. Liu, J. Y. Mao, B. F. Zhao, X. Y. Mao, L. C. Zhang, L. Y. Cheng, Y. G. Zhang, X. M. Sun, W. G. Cui, Secretory Fluid-Aggregated Janus Electrospun Short Fiber Scaffold for Wound Healing. *Small* **18**, (2022).
28. J. J. Li, C. R. Yang, C. Ma, J. F. Yang, S. E. Zhou, H. Wang, L. Wen, A self-adhesive breathable Janus fibrous membrane for electronic skins with long-term comfort and reliability. *Chem Eng J* **522**, (2025).
29. L. L. Qian, F. Jin, T. Li, Z. D. Wei, X. Y. Ma, W. Y. Zheng, N. Javanmardi, Z. Wang, J. Ma, C. T. Lai, W. Dong, T. Wang, Z. Q. Feng, Self-Adhesive and Self-Sustainable Bioelectronic Patch for Physiological Feedback Electronic Modulation of Soft Organs. *Adv Mater* **36**, (2024).
30. C. X. Shi, H. Wang, X. J. Wang, K. F. Li, P. B. Liu, L. H. Wang, H. Yu, A Safe, Stable, Simple, Serviceable, and Self-Powered Wound Dressing With Continuous Low-Voltage Direct Current Electrical Stimulation: an Efficient Approach to Accelerate Wound Healing. *Adv Funct Mater*, (2025).
31. S. C. Zhang, H. Liu, N. Tang, J. L. Ge, J. Y. Yu, B. Ding, Direct electronetting of high-performance membranes based on self-assembled 2D nanoarchitectured networks. *Nat Commun* **10**, (2019).
32. J. B. Ballengee, P. N. Pintauro, Morphological Control of Electrospun Nafion Nanofiber Mats. *J Electrochem Soc* **158**, B568-B572 (2011).
33. D. X. Ji, Y. G. Lin, X. Y. Guo, B. Ramasubramanian, R. W. Wang, N. Radacsi,

R. Jose, X. H. Qin, S. Ramakrishna, Electrospinning of nanofibres. *Nat Rev Method Prime* **4**, (2024).

34. A. Keirouz, Z. Wang, V. S. Reddy, Z. K. Nagy, P. Vass, M. Buzgo, S. Ramakrishna, N. Radacsi, The History of Electrospinning: Past, Present, and Future Developments. *Adv Mater Technol-Us* **8**, (2023).
35. L. H. Wu, Y. Q. Wang, X. Y. Zhao, T. T. Zhao, J. H. Li, Y. Kuang, Y. Y. He, S. X. Yang, Z. W. Gu, H. L. Mao, A self-adhesive hierarchical nanofiber patch for dynamic and multistage management of full-thickness cutaneous wounds. *J Nanobiotechnol* **23**, (2025).
36. H. Yu, Y. J. Li, Y. N. Pan, H. N. Wang, W. Wang, X. B. Ren, H. Yuan, Z. R. Lv, Y. J. Zuo, Z. R. Liu, W. Lin, Q. Q. Yao, Multifunctional porous poly (L-lactic acid) nanofiber membranes with enhanced anti-inflammation, angiogenesis and antibacterial properties for diabetic wound healing. *J Nanobiotechnol* **21**, (2023).
37. L. L. Sun, J. C. Wang, H. Matsui, S. Y. Lee, W. Q. Wang, S. Y. Guo, H. T. Chen, K. Fang, Y. Ito, D. Inoue, D. Hashizume, K. Mori, M. Takakuwa, S. H. Lee, Y. H. Zhou, T. Yokota, K. Fukuda, T. Someya, All-solution-processed ultraflexible wearable sensor enabled with universal trilayer structure for organic optoelectronic devices. *Sci Adv* **10**, (2024).
38. T. W. Kang, Y. J. Lee, B. Rigo, I. Soltis, J. Lee, H. Kim, G. R. Wang, N. Zavanelli, E. Ayesh, W. Sohail, H. Majditehran, S. H. Kozin, F. I. I. I. Hammond, W. H. Yeo, Soft Nanomembrane Sensor-Enabled Wearable Multimodal Sensing and Feedback System for Upper-Limb Sensory Impairment Assistance. *Acs Nano* **19**, 5613-5628 (2025).
39. L. Wu, X. Huang, M. Wang, J. S. Z. Chen, J. K. Chang, H. Zhang, X. T. Zhang, A. Conn, J. Rossiter, M. Birchall, W. H. Song, Tunable Light-Responsive Polyurethane-urea Elastomer Driven by Photochemical and Photothermal Coupling Mechanism. *Acs Appl Mater Inter* **16**, 19480-19495 (2024).
40. Y. Paez-Amieva, N. Mateo-Oliveras, J. M. Martín-Martínez, Polyurethanes Synthesized with Blends of Polyester and Polycarbonate Polyols-New Evidence Supporting the Dynamic Non-Covalent Exchange Mechanism of Intrinsic Self-Healing at 20 °C. *Polymers-Basel* **16**, (2024).
41. T. Laukkanen, P. G. Reddy, A. Barua, M. Kumar, K. Kolpakov, T. Tirri, V. Sharma, Sustainable castor oil-derived cross-linked poly(ester-urethane) elastomeric films for stretchable transparent conductive electrodes and heaters. *J Mater Chem A* **12**, 33177-33192 (2024).
42. H. R. Wang, L. Cao, X. L. Wang, X. R. Lang, W. W. Cong, L. Han, H. Y. Zhang, H. B. Zhou, J. J. Sun, C. Z. Zong, Effects of Isocyanate Structure on the Properties of Polyurethane: Synthesis, Performance, and Self-Healing Characteristics. *Polymers-Basel* **16**, (2024).
43. S. H. D. Wong, G. R. Deen, J. S. Bates, C. Maiti, C. Y. K. Lam, A. Pachauri, R. AlAnsari, P. Belsky, J. Yoon, J. M. Dodda, Smart Skin-Adhesive Patches: From Design to Biomedical Applications. *Adv Funct Mater* **33**, (2023).
44. Y. Zhou, L. N. Yang, Z. Liu, Y. Sun, J. F. Huang, B. C. Liu, Q. Wang, L. Y.

Wang, Y. Miao, M. L. Xing, Z. Q. Hu, Reversible adhesives with controlled wrinkling patterns for programmable integration and discharging. *Sci Adv* **9**, (2023).

45. C. Lim, Y. J. Hong, J. Jung, Y. Shin, S. H. Sunwoo, S. Baik, O. K. Park, S. H. Choi, T. Hyeon, J. H. Kim, S. Lee, D. H. Kim, Tissue-like skin-device interface for wearable bioelectronics by using ultrasoft, mass-permeable, and low-impedance hydrogels. *Sci Adv* **7**, (2021).
46. Z. X. Yang, K. X. Ren, Y. H. Chen, X. Y. Quanji, C. F. Cai, J. B. Yin, Oxygen-Generating Hydrogels as Oxygenation Therapy for Accelerated Chronic Wound Healing. *Adv Healthc Mater* **13**, (2024).
47. K. R. Kleinbeck, R. A. Bader, W. J. Kao, Concurrent In Vitro Release of Silver Sulfadiazine and Bupivacaine From Semi-Interpenetrating Networks for Wound Management. *J Burn Care Res* **30**, 98-104 (2009).
48. C. Bergonzi, A. Bianchera, G. Remaggi, M. C. Ossiprandi, R. Bettini, L. Elviri, 3D Printed Chitosan/Alginate Hydrogels for the Controlled Release of Silver Sulfadiazine in Wound Healing Applications: Design, Characterization and Antimicrobial Activity. *Micromachines-Basel* **14**, (2023).
49. W. K. Jung, H. C. Koo, K. W. Kim, S. Shin, S. H. Kim, Y. H. Park, Antibacterial activity and mechanism of action of the silver ion in Staphylococcus aureus and Escherichia coli. *Appl Environ Microb* **74**, 2171-2178 (2008).
50. C. Z. Liao, Y. C. Li, S. C. Tjong, Bactericidal and Cytotoxic Properties of Silver Nanoparticles. *Int J Mol Sci* **20**, (2019).
51. Y. N. Zhu, J. M. Zhang, J. Y. Song, J. Yang, Z. Du, W. Q. Zhao, H. S. Guo, C. Y. Wen, Q. S. Li, X. J. Sui, L. Zhang, A Multifunctional Pro-Healing Zwitterionic Hydrogel for Simultaneous Optical Monitoring of pH and Glucose in Diabetic Wound Treatment. *Adv Funct Mater* **30**, (2020).
52. X. C. Huang, J. R. Zhang, L. L. Zhang, H. Su, X. M. Liu, J. Liu, A sensitive H_2O_2 biosensor based on carbon nanotubes/tetrathiafulvalene and its application in detecting NADH. *Anal Biochem* **589**, (2020).
53. B. Mecheri, D. De Porcellinis, P. T. Campana, A. Rainer, M. Trombetta, A. Marletta, O. N. Oliveira, S. Licoccia, Tuning Structural Changes in Glucose Oxidase for Enzyme Fuel Cell Applications. *Acs Appl Mater Inter* **7**, 28311-28318 (2015).
54. J. J. Garcia-Guzmán, J. M. J. Heras, D. López-Iglesias, R. J. Gonzalez-alvarez, L. Cubillana-Aguilera, C. G. Macias, J. J. F. Alba, J. M. Palacios-Santander, New spin coated multilayer lactate biosensor for acidosis monitoring in continuous flow assisted with an electrochemical pH probe. *Microchim Acta* **191**, (2024).
55. Y. Lyu, P. Mollik, A. L. Olah, D. P. Halter, Construction and Evaluation of Cheap and Robust Miniature Ag/AgCl Reference Electrodes for Aqueous and Organic Electrolytes. *Chemelectrochem* **11**, (2024).
56. J. Leal, S. Shaner, N. Jedrusik, A. Savelyeva, M. Asplund, Electrotaxis evokes directional separation of co-cultured keratinocytes and fibroblasts. *Sci Rep-Uk*

13, (2023).

57. B. Song, M. Zhao, J. V. Forrester, C. D. McCaig, Electrical cues regulate the orientation and frequency of cell division and the rate of wound healing. *Proceedings of the National Academy of Sciences of the United States of America* **99**, 13577-13582 (2002).
58. K. Nakajima, K. Zhu, Y. H. Sun, B. Hegyi, Q. L. Zeng, C. J. Murphy, J. V. Small, C. I. Ye, Y. Izumiya, J. M. Penninger, M. Zhao, /Kir4.2 couples with polyamines to sense weak extracellular electric fields in galvanotaxis. *Nat. Commun.* **6**, (2015).
59. B. J. Lin, S. H. Tsao, A. Chen, S. K. Hu, L. Chao, P. H. G. Chao, Lipid rafts sense and direct electric field-induced migration. *P Natl Acad Sci USA* **114**, 8568-8573 (2017).
60. R. Kaveti, M. A. Jakus, H. Chen, B. Jain, D. G. Kennedy, E. A. Caso, N. Mishra, N. Sharma, B. E. Uzunoglu, W. B. Han, T. M. Jang, S. W. Hwang, G. Theocharidis, B. J. Sumpio, A. Veves, S. K. Sia, A. J. Bandodkar, Water-powered, electronics-free dressings that electrically stimulate wounds for rapid wound closure. *Sci Adv* **10**, (2024).
61. R. Z. Luo, Y. Liang, J. R. Yang, H. Q. Feng, Y. Chen, X. P. Jiang, Z. Zhang, J. Liu, Y. Bai, J. T. Xue, S. Y. Chao, Y. Xi, X. Q. Liu, E. G. Wang, D. Luo, Z. Li, J. P. Zhang, Reshaping the Endogenous Electric Field to Boost Wound Repair via Electrogenerative Dressing. *Adv Mater* **35**, (2023).
62. E. Maslova, L. EisaianKhongi, P. Rigole, T. Coenye, R. R. McCarthy, Carbon source competition within the wound microenvironment can significantly influence infection progression. *Npj Biofilms Microbi* **10**, (2024).
63. E. Khatib-Massalha, S. Bhattacharya, H. Massalha, A. Biram, K. Golan, O. Kollet, A. Kumari, F. Avemaria, E. Petrovich-Kopitman, S. Gur-Cohen, T. Itkin, I. Brandenburger, A. Spiegel, Z. Shulman, Z. Gerhart-Hines, S. Itzkovitz, M. Gunzer, S. Offermanns, R. Alon, A. Ariel, T. Lapidot, Lactate released by inflammatory bone marrow neutrophils induces their mobilization via endothelial GPR81 signaling. *Nat Commun* **11**, (2020).
64. X. Zhao, J. H. Huang, J. C. Zhang, B. W. Yang, Z. J. Hu, T. Li, X. Ma, C. Y. Jiang, H. C. Zou, S. R. Liu, Q. S. He, L. X. Weng, T. Wang, L. H. Wang, Soft bioelectronics embedded with self-confined tetrahedral DNA circuit for high-fidelity chronic wound monitoring. *Nat Commun* **16**, (2025).
65. H. L. Haller, F. Sander, D. Popp, M. Rapp, B. Hartmann, M. Demircan, S. P. Nischwitz, L. P. Kamolz, Oxygen, pH, Lactate, and Metabolism-How Old Knowledge and New Insights Might Be Combined for New Wound Treatment. *Medicina-Lithuania* **57**, (2021).
66. C. Dunker, M. Polke, B. Schulze-Richter, K. Schubert, S. Rudolphi, A. E. Gressler, T. Pawlik, J. P. Prada Salcedo, M. J. Niemiec, S. Slesiona-Künzel, M. Swidergall, R. Martin, T. Dandekar, I. D. Jacobsen, Rapid proliferation due to better metabolic adaptation results in full virulence of a filament-deficient strain. *Nat Commun* **12**, (2021).

Supplementary Materials for

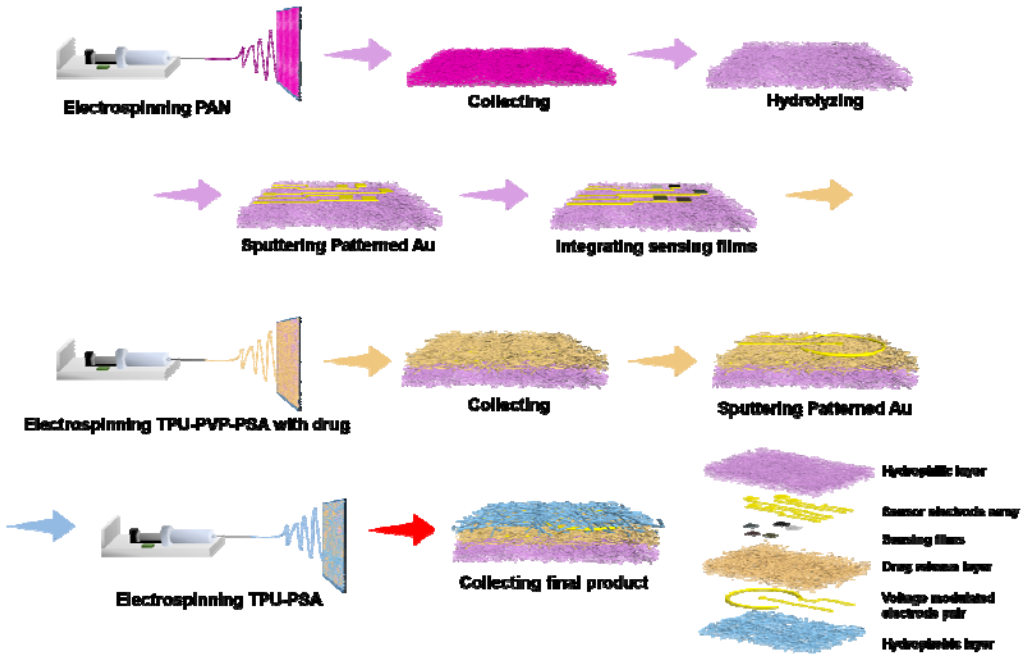

Figure S1. The fabrication process of the bioelectronic wound dressing.

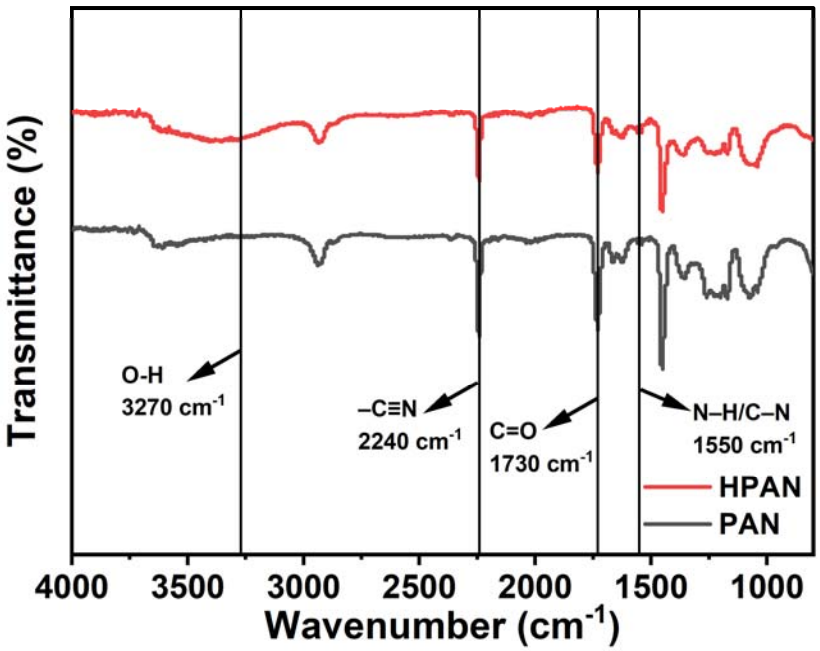

Figure S1. FT-IR spectra of pristine PAN and hydrolyzed HPAN.

Key spectral transitions confirm successful hydrolysis/ Emergence of broad O-H stretch at 3270 cm□¹, enhanced C=O stretch at 1730 cm□¹ (carboxylic acid formation) and Characteristic amide II band at 1550 cm□¹ (coupled N-H bending and C-N stretching), and concomitant reduction in -C≡N peak intensity at 2240 cm□¹ (nitrile group consumption). This collective shift verifies the generation of hydrophilic hydroxyl/carboxyl functionalities at the expense of hydrophobic nitrile groups, directly correlating with the significantly enhanced hydrophilicity of HPAN.

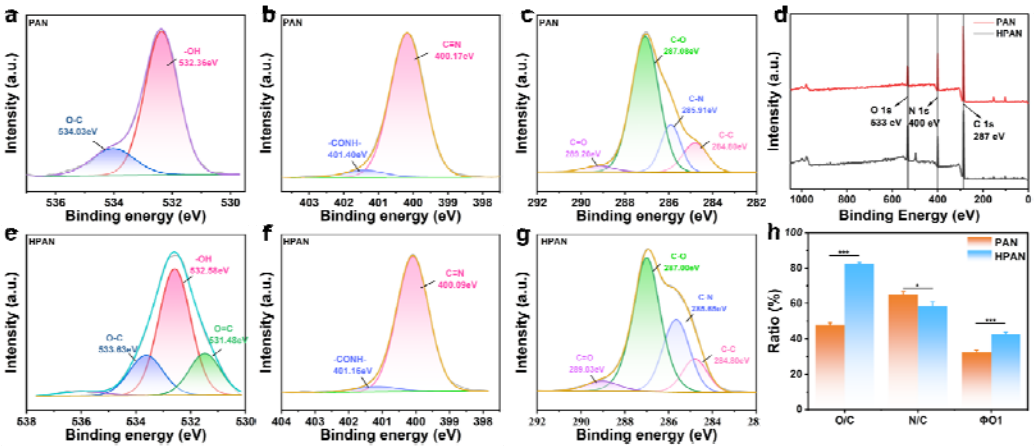

Figure S3. XPS analysis of PAN and hydrolyzed HPAN. (a-c) High-resolution XPS spectra of pristine PAN showing the (a) O 1s, (b) N 1s, and (c) C 1s core levels. (d-f) High-resolution XPS spectra of HPAN showing the (d) O 1s, (e) N 1s, and (f) C 1s core levels. (g) Survey scan spectra comparing the elemental composition of pristine PAN and HPAN. (h) Quantitative analysis of elemental composition ratios (O/C, N/C) and O 1s chemical state changes (φO1, representing the fraction of C=O plus C–O/–OH species relative to total O 1s peak area) induced by hydrolysis.

Core-level XPS spectra document the hydrolysis-induced chemical transformation: The O 1s spectrum of pristine PAN (Figure S2a) exhibits characteristic peaks at 532.36 eV (hydroxyl groups) and 534.03 eV (ether-type oxygen), while its N 1s spectrum (Figure S2 b) shows signatures at 400.17 eV (nitrile nitrogen) and 401.40 eV (amide nitrogen). Corresponding C 1s signals (Figure S2c) appear at 284.80 eV (aliphatic carbon), 285.91 eV (carbon-nitrogen bonds), 287.08 eV (alcohol/ether carbon), and 289.20 eV (carbonyl carbon). Following hydrolysis, HPAN demonstrates significant chemical shifts: The O 1s spectrum (Figure S2e) displays new components at 531.48 eV (carboxylic oxygen) alongside modified peaks at 532.58 eV (hydroxyl) and 534.63 eV (ether oxygen); the N 1s spectrum (Figure S2f) shows attenuated nitrile intensity at 400.10 eV with persistent amide contribution at 401.16 eV; the C 1s spectrum (Figure S2g) maintains the carbon skeleton signal at 284.80 eV but reveals chemical environment alterations at 285.65 eV (C-N), 287.00 eV (C-O), and 289.03 eV (C=O). Full-survey spectra (Figure S2d) confirm elemental

redistribution: nitrogen signal attenuation directly attributable to nitrile group consumption contrasts with oxygen signal enhancement from newly generated hydroxyl and carboxyl functionalities, while carbon peak broadening indicates heteroatom incorporation into the polymer backbone. Quantitative analysis (Figure S2h) reveals substantially increased oxygen-to-carbon atomic ratio and elevated proportion of polar carbonyl/hydroxyl groups within O 1s spectra, coupled with decreased nitrogen-to-carbon ratio, collectively evidencing successful conversion of hydrophobic nitriles to hydrophilic moieties that significantly enhance surface wettability.

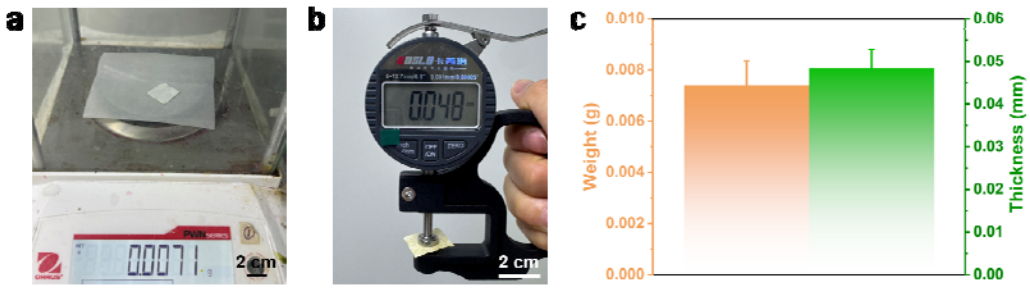

Figure S4. Photograph images of the trilayer (a) with a total weight of 0.0071 g (b) and thickness of 0.048 mm. (c) Average weight and thickness of trilayer. The dimensions of the samples were fixed as 2 cm by 2 cm. Error bars represent mean ± SD (n=3).

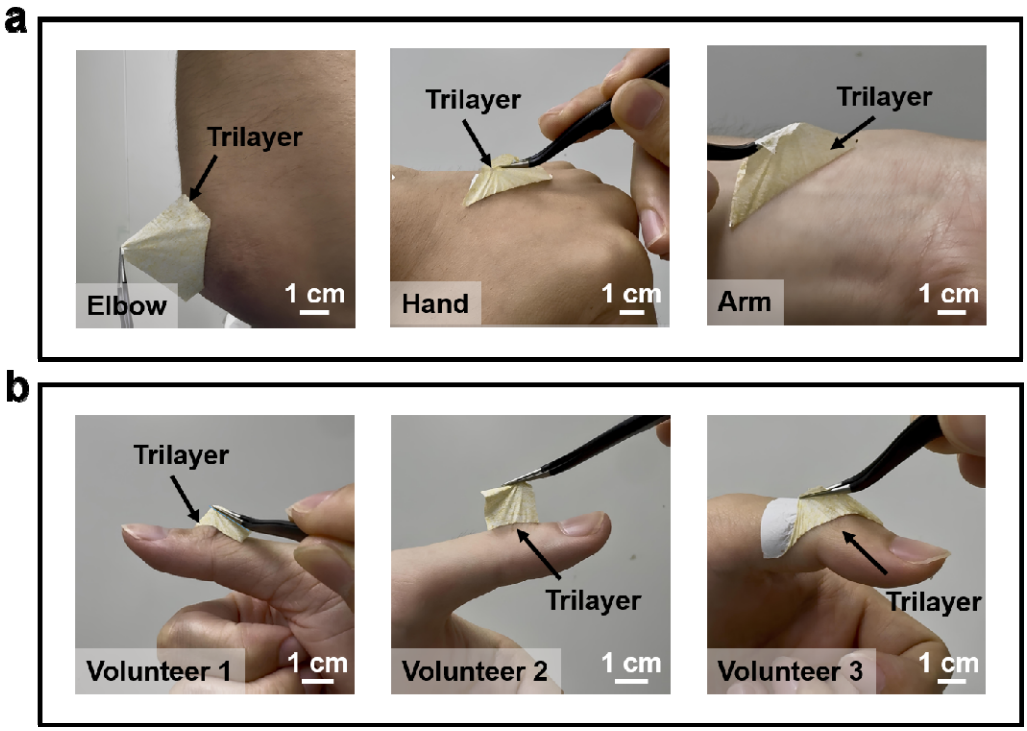

Figure S5. Surface adhesion properties of the trilayer membrane. Photos showing the trilayer membrane detached from (a) different parts of the body (b) and the finger

joints of different volunteers without any harms.

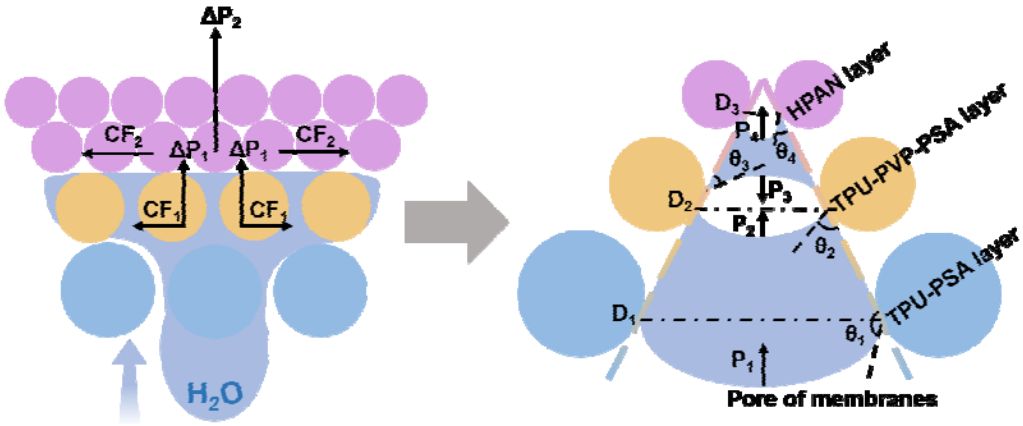

Figure S6. Diagram of the simplified mechanism of passive wicking process of trilayer membrane.

When a water droplet initially contacts the trilayer membrane, it rapidly infiltrates into the inter-fiber capillary channels of the hydrophobic TPU-PSA layer due to localized wetting at fiber junctions. Subsequently, the liquid is subjected to Laplace pressure, described as:

$$P = (4\gamma\cos\theta)/D$$

Where γ is the liquid–gas interfacial tension, θ is the contact angle on the fiber surface, and D is the effective pore diameter between adjacent fibers. According to this relation, both increasing wettability (decreasing θ) and decreasing pore size (smaller D) contribute to a higher capillary pressure. Thus, a net upward driving force is established across the membrane.

At the interface between the TPU-PSA and TPU-PVP-PSA layers, the water droplet experiences two Laplace pressures, P_1 and P_2, acting in the same direction. The resulting pressure gradient ΔP_1 is:

$$\Delta P_1 = (4\gamma\cos\theta_2)/D_2 - (4\gamma\cos\theta_1)/D_1$$

Where θ_1 and θ_2 are the contact angles of the TPU-PSA and TPU-PVP-PSA layers, respectively, and D_1 and D_2 are their corresponding pore sizes. A similar expression holds at the interface between TPU-PVP-PSA and HPAN layers, generating a secondary pressure gradient $\Delta P_2 = P_4 - |P_3|$ which further supports upward

liquid transport, albeit at a reduced magnitude. This staged pressure difference ensures a sustained and directional movement of fluid through the membrane.

Importantly, the TPU-PSA hydrophobic layer serves as an effective barrier against external contaminants, preventing reverse penetration. Meanwhile, the TPU-PVP-PSA layer retains fluid temporarily, allowing for absorption and controlled swelling, while the hydrophilic HPAN layer promotes rapid evaporation or outward release.

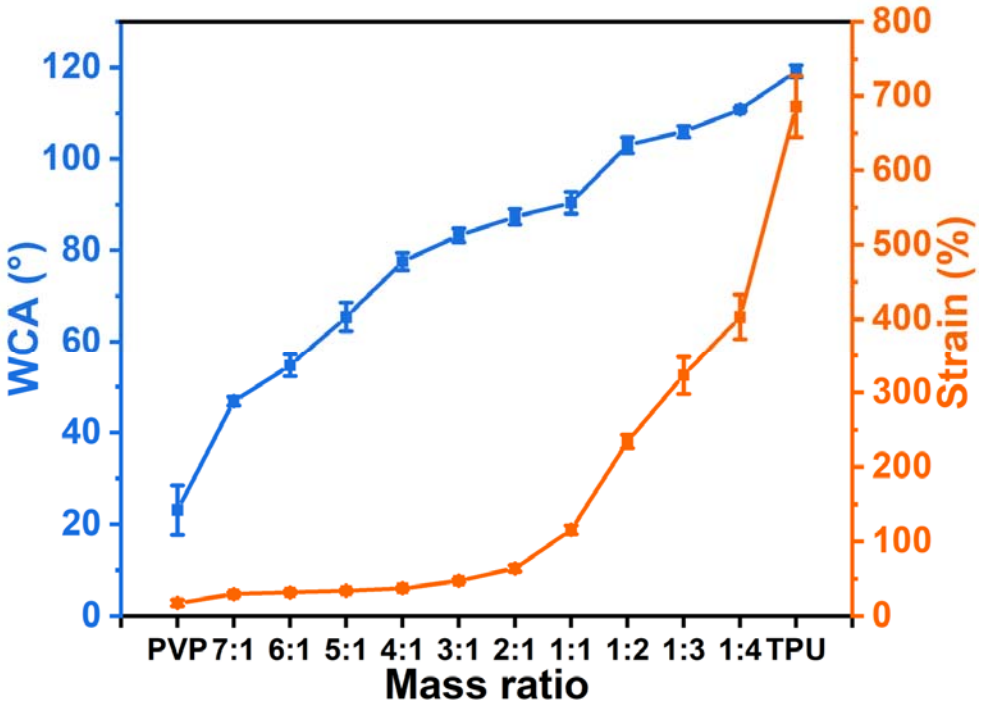

Figure S7. The water contact angel and strain of different mass ratio of PVP and TPU. Error bars represent mean ± SD (n=3).

Figure S6 demonstrates the inverse correlation between PVP content and membrane properties. Higher hydrophilic PVP fractions reduce initial water contact angles, enhancing hydrophilicity but diminishing strain capacity. Conversely, increased hydrophobic TPU content improves extensibility while elevating contact angles. To achieve both graded wettability and reduced Young's modulus in the trilayer system, a 1:1 TPU to PVP ratio was selected. This formulation yields a 90.44° contact angle and 115.73% strain capacity. These intermediate values bridge the hydrophilic outer layer and hydrophobic inner layer, establishing hydraulic continuity for directional fluid transport without sacrificing mechanical compliance.。

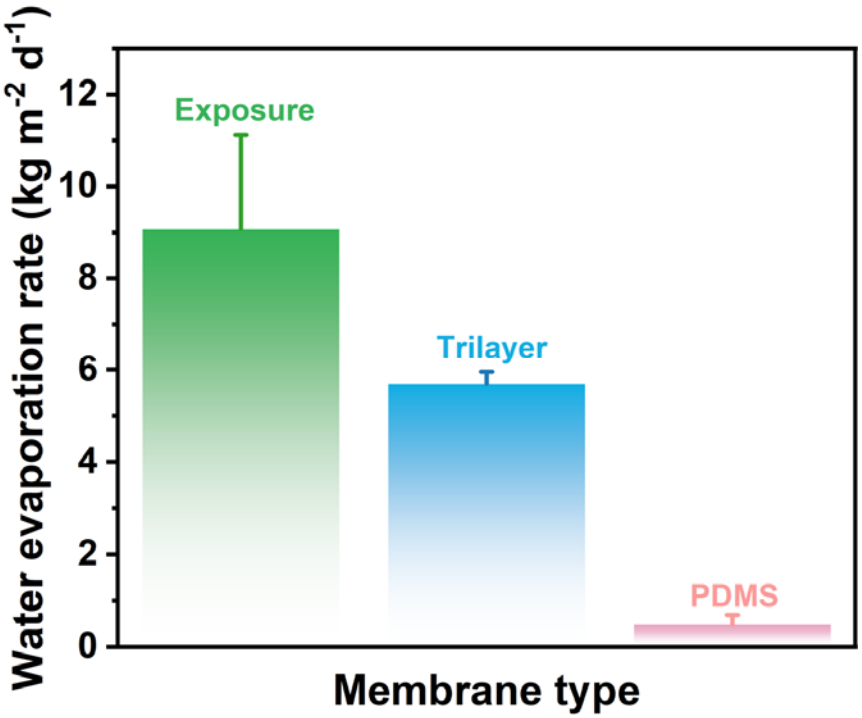

Figure S8. Statistical results of quantitative data on the breathability of the trilayer membrane. Error bars represent mean ± SD (n=3).

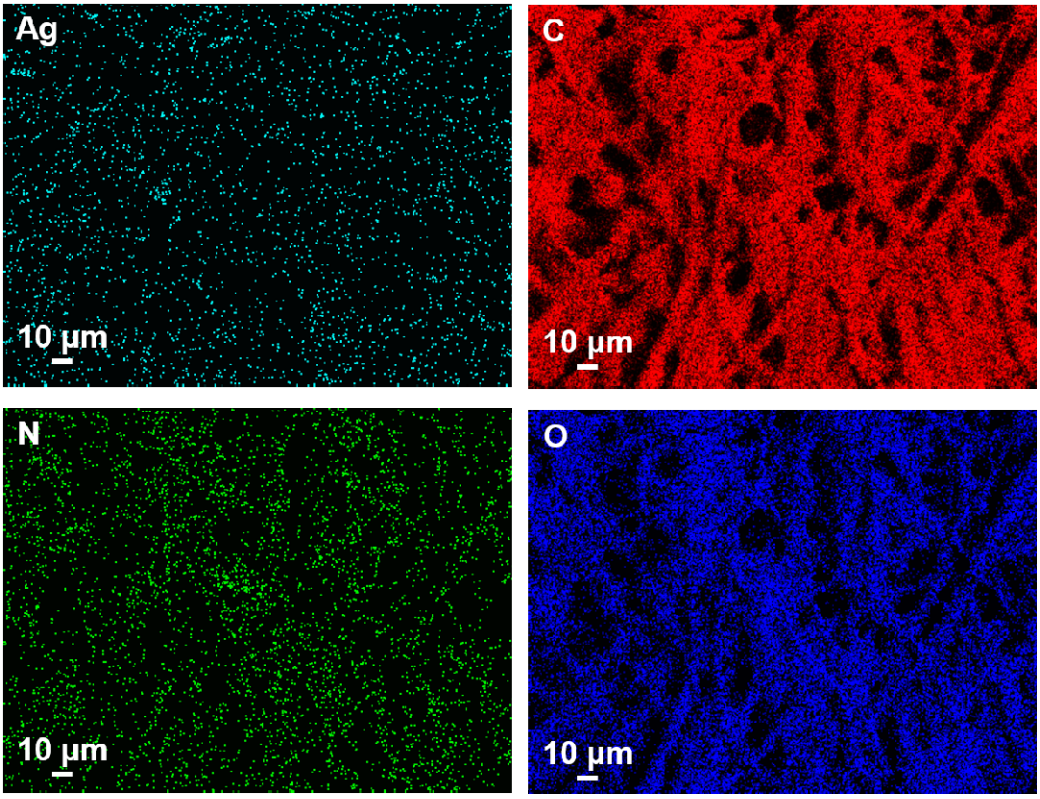

Figure S9. EDS mapping of TPU-PVP-PSA layer with silver sulfadiazine.

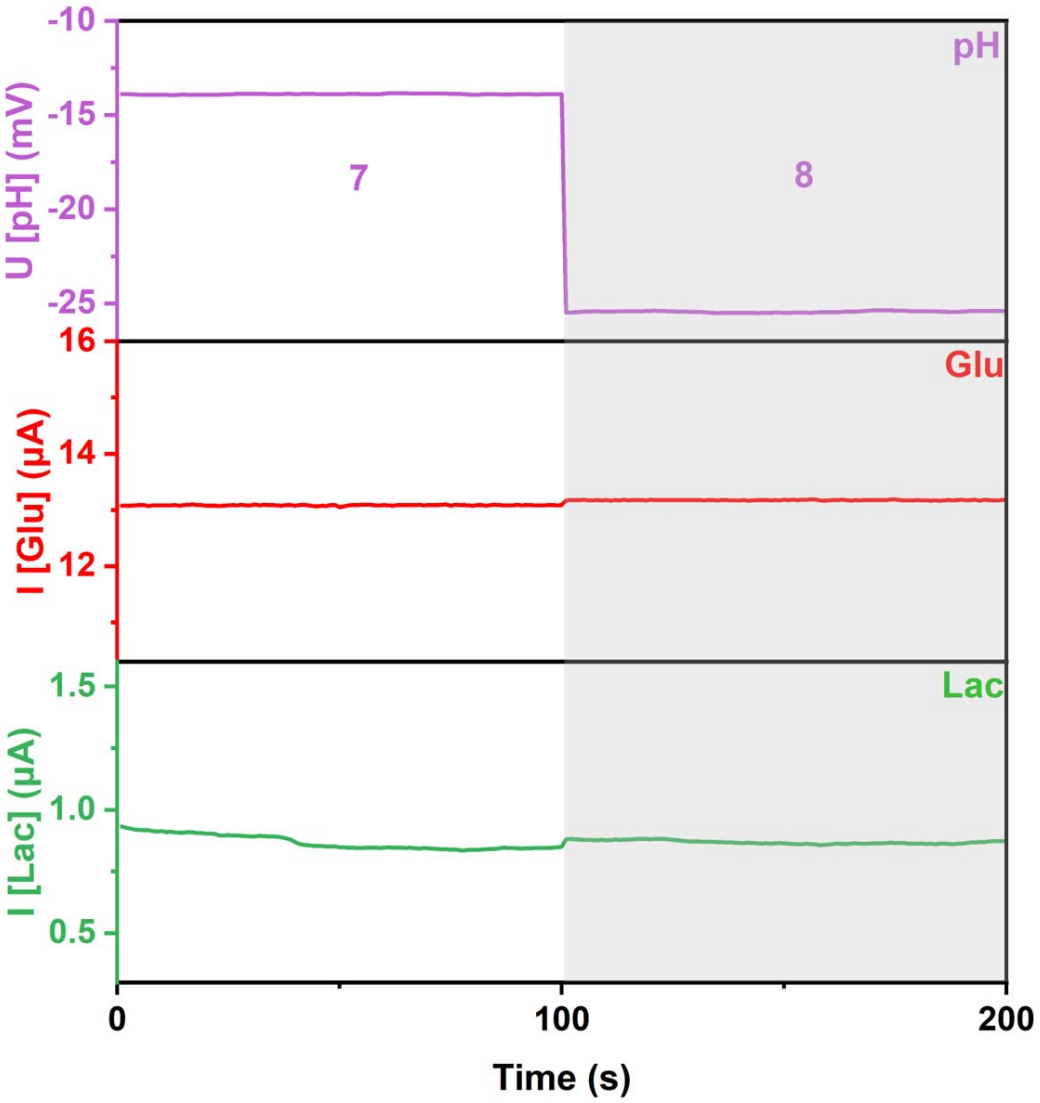

Figure S10. The influence of pH on the responses of sensors. Test solutions included pH 7.0 and 8.0 standard buffers with 10 mM glucose and 1 mM lactate.

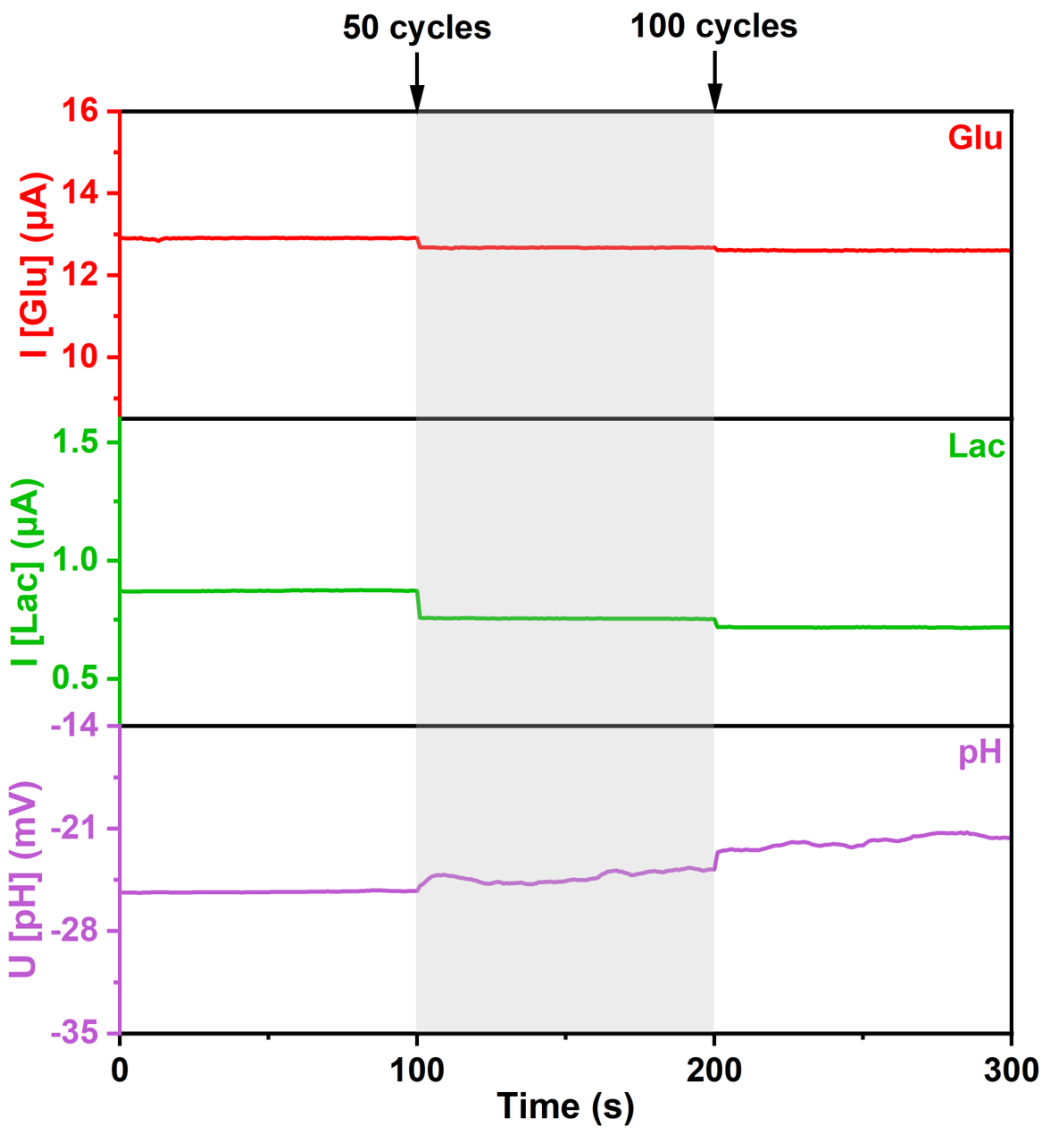

Figure S11. The operation stability of the sensors. Data was recorded before and after 50 and 100 cycles of repetitive operation. Test solutions included 10 mM glucose solution, 1 mM lactate solution and pH 8.0 standard buffer.

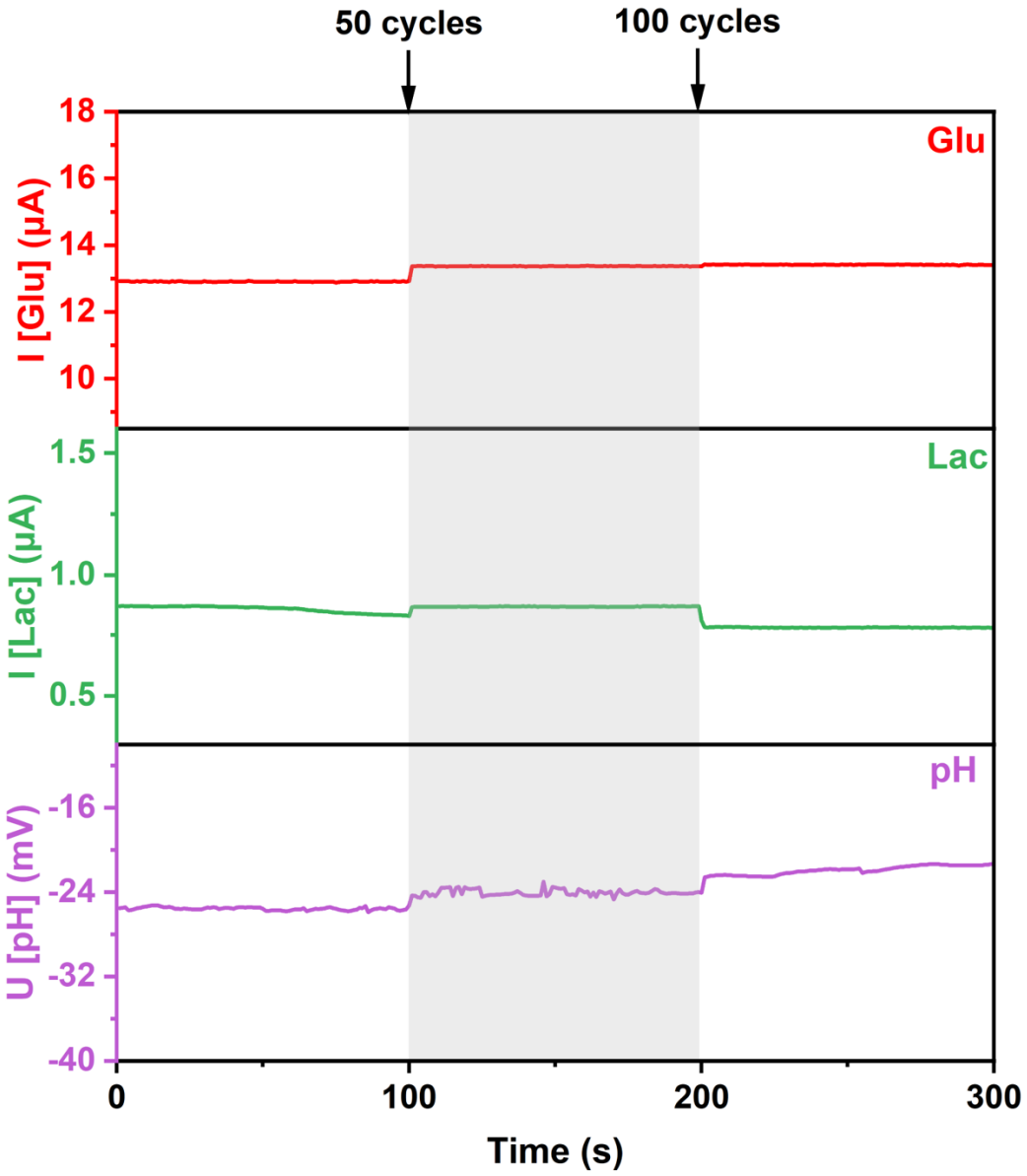

Figure S12. The mechanical stability of the sensors. Data was recorded before and after 50 and 100 cycles of repetitive mechanical bending (radius of curvature, 1 cm). Test solutions included 10 mM glucose solution, 1 mM lactate solution and pH 8.0 standard buffer.

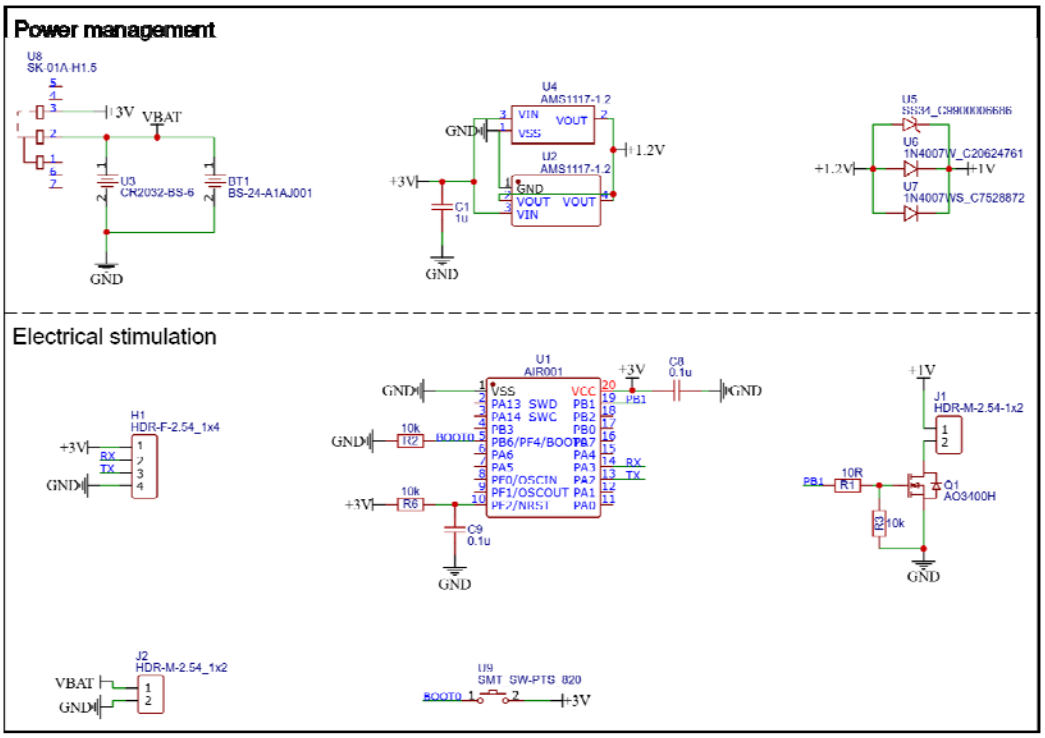

Figure S13. Circuit diagram of the electrical stimulation system.

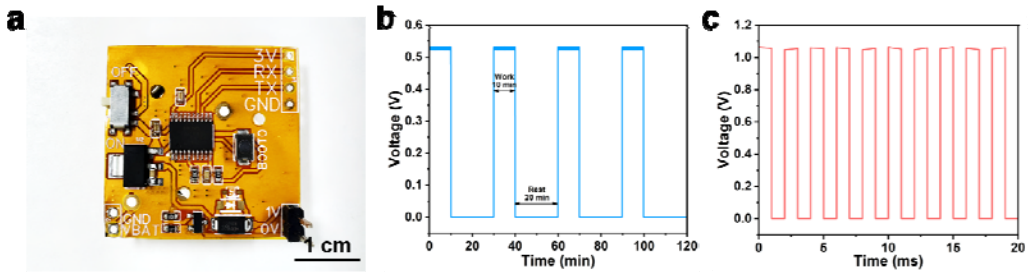

Figure S14. (a) Optical image of the electrical stimulation system integrated on a flexible printed circuit board (FPCB). (b) Voltage profile showing the programmed working mode of the system, consisting of a 10-minute stimulation phase followed by a 20-minute rest period. (c) Representative stimulation waveform during the working phase, delivering a 1 V, 50 Hz signal.

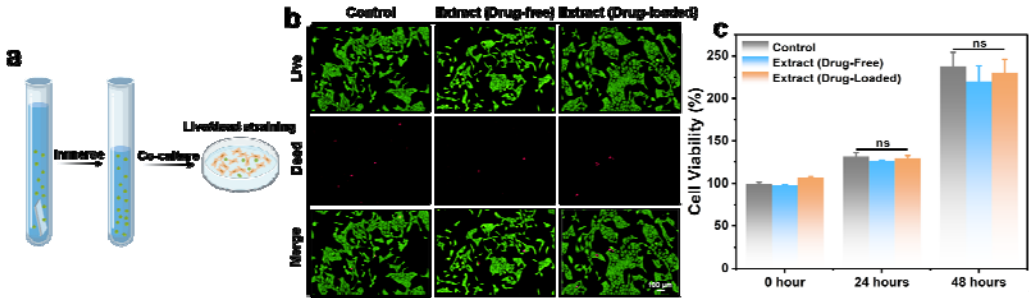

Figure S15. In vitro evaluation of the biocompatibility of the trilayer membrane. a) Schematic illustration of the preparation of the membrane extract used for live/dead staining. b) Live/dead fluorescence images of the control group, extract (drug-free), and extract (drug-loaded) after 48 hours of culture. c) CCK-8 cytotoxicity test of the various groups at the time points of 0, 24, and 48 hours (n = 3).

We evaluated the biocompatibility of the trilayer membrane to assess its potential risks in biomedical applications. NIH-3T3 fibroblasts were co-cultured with the membrane extract to examine cytocompatibility (Figure S16a). After 48 hours of incubation in three groups (control, extract without drug, and extract with drug), the cells were subjected to live/dead staining and imaged using fluorescence microscopy (Figure S16b). As expected, only a small number of dead cells (red) were observed among the abundant live cells (green), and no apparent differences in cell morphology or viability were detected among the groups. To further quantify cell viability, optical density values were measured using the Cell Counting Kit-8 (CCK-8). As shown in Figure S16c, no significant differences were found among the groups during the 48-hour culture period, indicating that the drug-loaded membrane did not exhibit cytotoxicity.

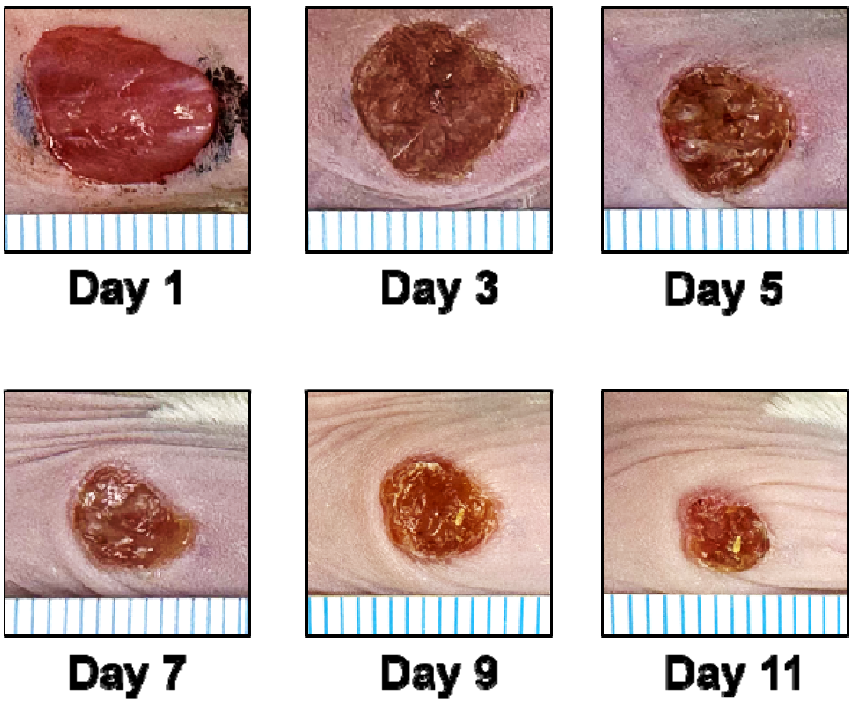

Figure S16. Representative photographs showing the wound healing progression over 11 days in the control group.

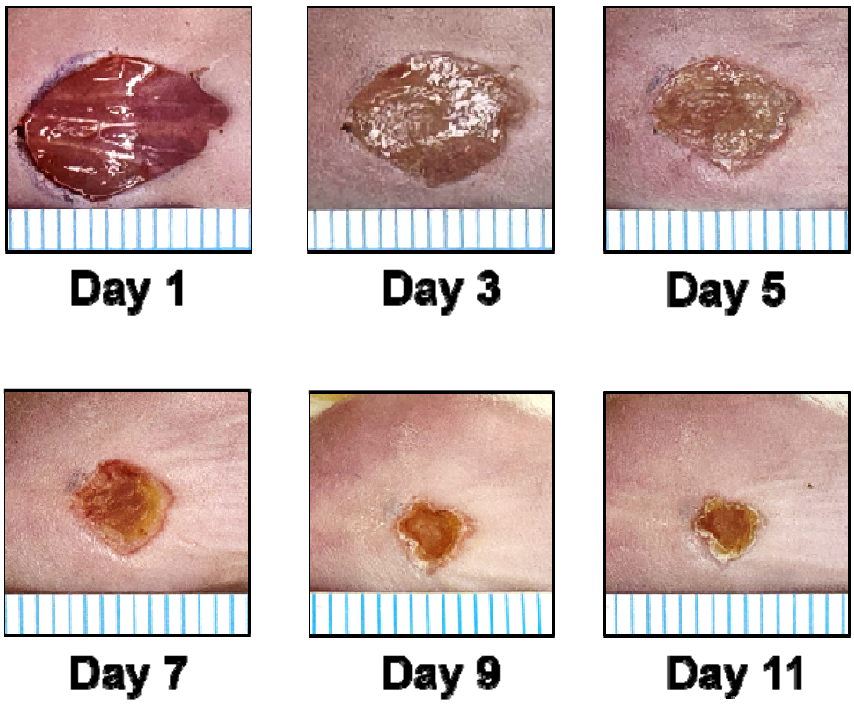

Figure S17. Representative photographs showing the wound healing progression over 11 days in the drug-only dressing group.

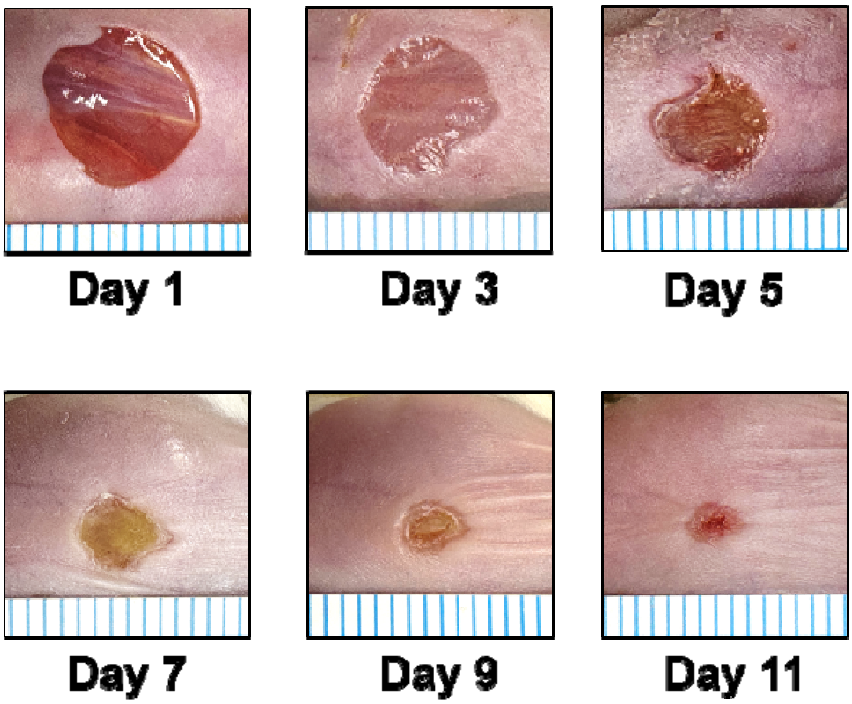

Figure S18. Representative photographs showing the wound healing progression over 11 days in the drug & ES dressing group.

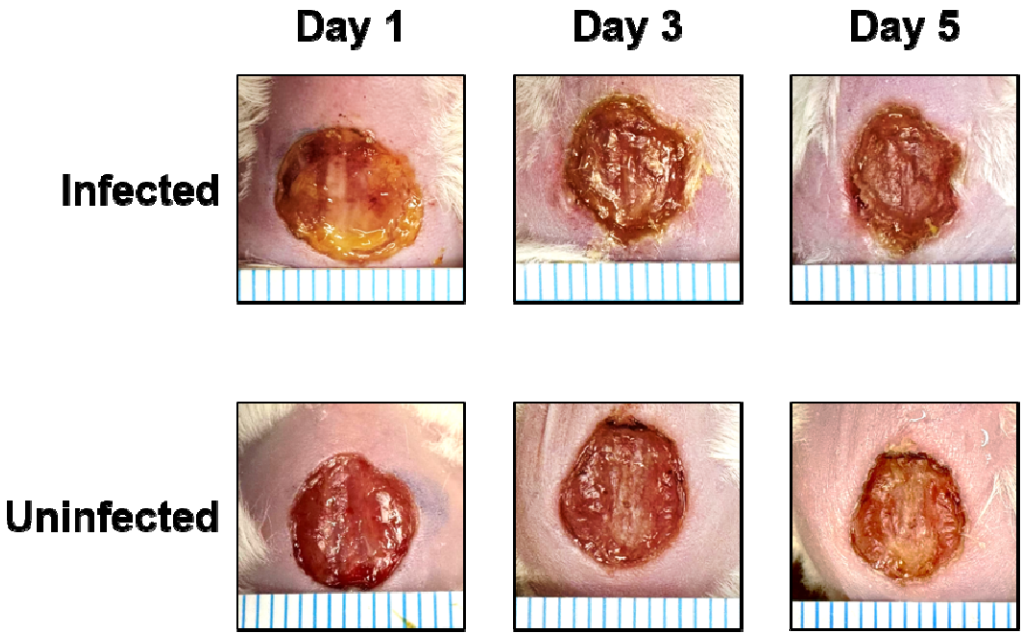

Figure S19. Representative photographs showing the wound healing progression at days 1, 3, and 5 in the infected and uninfected groups.

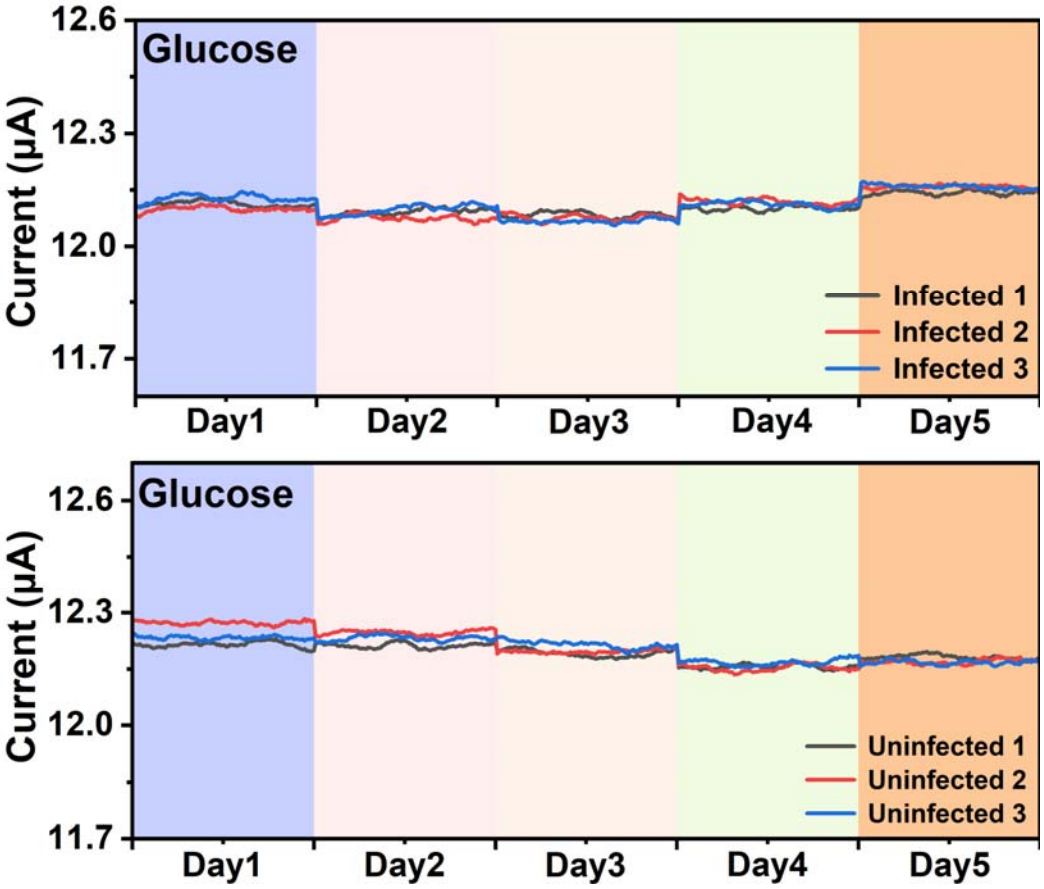

Figure S20. Glucose sensor signal changes over 5 consecutive days in the infected and uninfected groups under resting conditions.

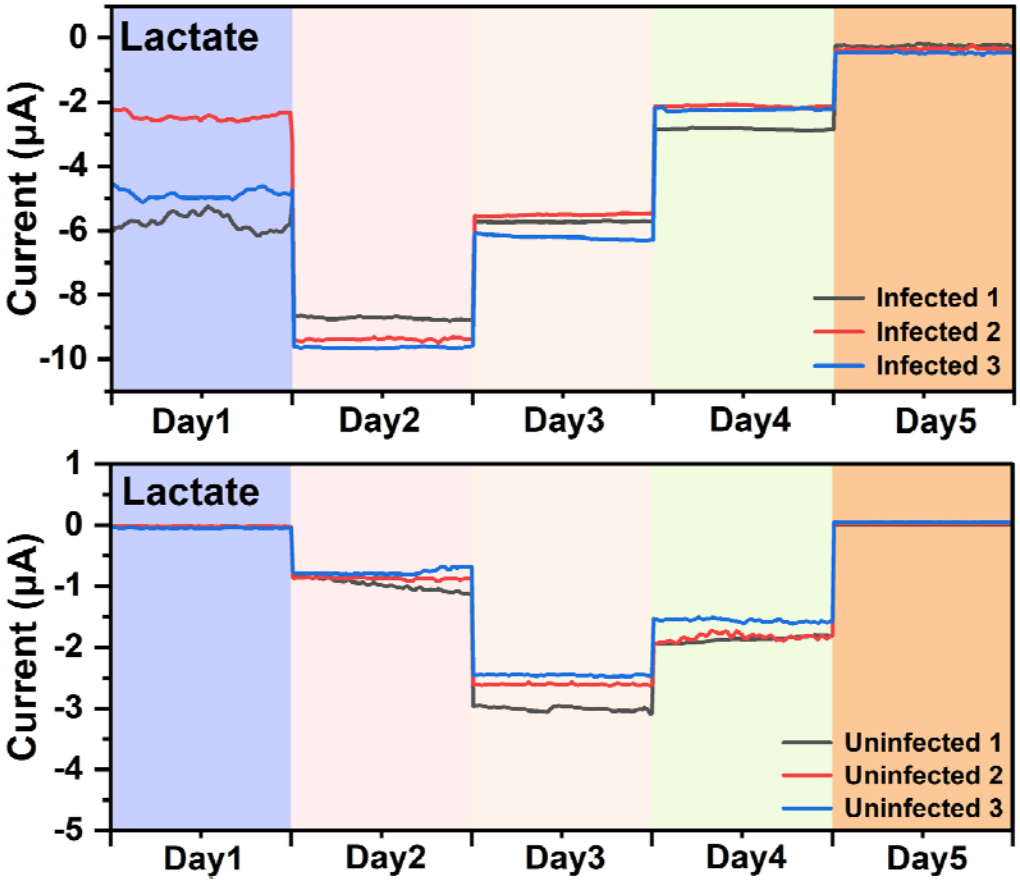

Figure S21. Lactate sensor signal changes over 5 consecutive days in the infected and uninfected groups under resting conditions.

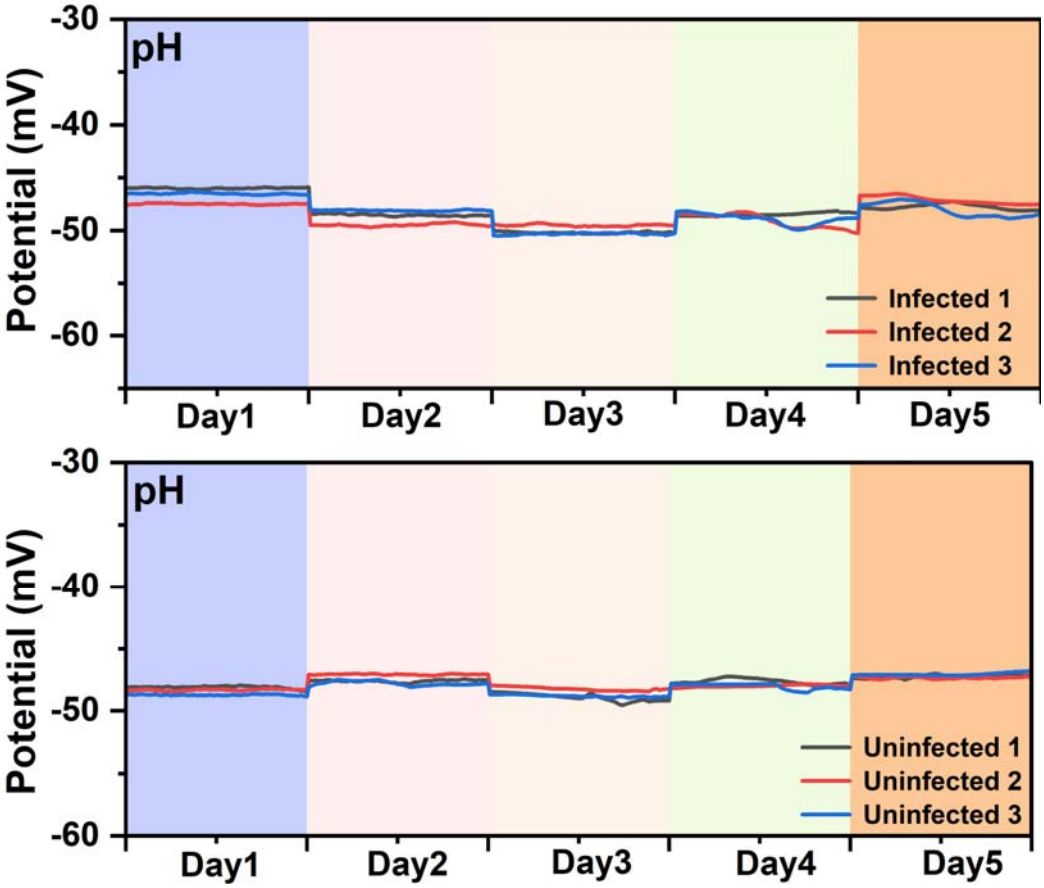

Figure S22. pH sensor signal changes over 5 consecutive days in the infected and uninfected groups under resting conditions.